Chapter 16

Resonators with Internal Nonlinear Elements

16.1 General Aspects

So far, we assumed that the optical materials inside the resonator exhibit an index of refraction that does not depend on the intensity of the incident light. This is a reasonable assumption as long as the light intensity is low. However, for high intensities the index of refraction n becomes a function of the incident field E (for symplifying the discussion we consider a real, scalar field):

$$n^2(E) = 1 + \chi^{(1)} + \chi^{(2)}E + \chi^{(3)}E^2 + \ldots \tag{16.1}$$

where $\chi^{(m)}$ is the m-th order susceptibility of the medium. This expansion of the refractive index holds for all optical materials, but for most materials the higher order susceptibilities are too small to have a noticeable effect on the electric field. However, some crystals exhibit relatively large susceptibilities on the order of 10^{-12} m/V for $\chi^{(2)}$ and 10^{-20} m^2/V^2 for $\chi^{(3)}$. These materials, which are referred to as nonlinear materials, are used to generate a variety of nonlinear effects. Second order effects (generated by $\chi^{(2)}$) include frequency doubling, sum and difference frequency generation, and parametric amplification, to name a few. Among third order effects are frequency tripling, self focusing, and stimulated Brillouin scattering. These nonlinear effects become more understandable if we consider the electric polarization P for an incident field E :

$$P = P^{(1)} + P^{(2)} + P^{(3)} + \ldots = \epsilon_0 (\chi^{(1)}E + \chi^{(2)}E^2 + \chi^{(3)}E^3 + \ldots) \tag{16.2}$$

with $\epsilon_0 = 8.854 \times 10^{-12}$ *As/(Vm)*. If two monochromatic fields E_1, E_2 propagating in the z-direction are incident on the nonlinear material, with:

$$E = E_1 + E_2 = E_{10} \sin[k_1 z - \omega_1 t] + E_{20} \sin[k_2 z - \omega_2 t] \tag{16.3}$$

the second order susceptibility $\chi^{(2)}$ generates, besides a constant offset, oscillating components of the dielectric polarization $P^{(2)}$ at the frequencies ω_1, ω_2, $2\omega_1$, $2\omega_2$, $\omega_1+\omega_2$, and $\omega_1-\omega_2$. In the following we restrict our discussion to those two nonlinear effects that are applied in laser resonators and induce a change of the light frequency; intracavity second harmonic generation (ICSHG), intracavity sum frequency generation, and phase conjugation via stimulated Brillouin scattering (SBS).

16.2 Intracavity Second Harmonic Generation

16.2.1 Basic Properties of SHG

We have seen that frequency doubling, also referred to as second harmonic generation, is generated by the second order susceptibility. If we consider a vector field $\boldsymbol{E}=(E_x,E_y,E_z)$, the second order dielectric polarization $\boldsymbol{P}^{(2)}$ can be written as:

$$\boldsymbol{P}^{(2)}=\begin{pmatrix}P_x^{(2)}\\P_y^{(2)}\\P_z^{(2)}\end{pmatrix}=\epsilon_0\begin{pmatrix}d_{11}&d_{12}&d_{13}&d_{14}&d_{15}&d_{16}\\d_{21}&d_{22}&d_{23}&d_{24}&d_{25}&d_{26}\\d_{31}&d_{32}&d_{33}&d_{34}&d_{35}&d_{36}\end{pmatrix}\begin{pmatrix}E_x^2\\E_y^2\\E_z^2\\2E_yE_z\\2E_xE_z\\2E_xE_y\end{pmatrix} \tag{16.4}$$

with $\epsilon_0=8.85\cdot10^{-12}$As/(Vm). For loss-free materials, only 10 of the 18 nonlinearity coefficients d_{ij} are independent (Kleinman symmetry relations). Furthermore, depending on the symmetry of the crystal, the number of independent coefficients is considerably reduced so that for most SHG crystals only two or three independent, nonzero coefficients remain (Table 16.1). In centro-symmetric crystals all coefficients equal zero, which means that these materials cannot generate second order nonlinear effects, except at the surface.

Table 16.1 Nonzero nonlinear coefficients d_{mn} of some materials [4.142].

Material	d_{mn} [10^{-12}m/V]	fundamental wavelength λ [μm]
KDP (KH_2PO_4)	$d_{36}\approx d_{25}=d_{14}=0.39\pm0.1$	1.06
KD*P (KD_2PO_4)	$d_{36}\approx d_{25}=d_{14}=0.40\pm0.17$	1.06
AD*P ($NH_2D_2PO_4$)	$d_{36}\approx d_{25}=d_{14}=0.52\pm0.08$	0.69
KDA (KH_2AsO_4)	$d_{36}\approx d_{25}=d_{14}=0.52\pm0.03$	0.69
LBO (LiB_3O_5)	$d_{31}=d_{32}=d_{15}=d_{24}=\pm(1.1\pm0.09)$ $d_{33}=0.06\pm0.006$	1.06
$LiNbO_3$	$d_{15}=d_{24}=d_{32}=d_{31}=-5.5\pm0.2$ $d_{16}=d_{21}=-d_{22}=-2.76\pm0.1$, $d_{33}=-34.4\pm2$	1.06
BBO (β-BaB_2O_4)	$d_{15}=d_{24}=d_{32}=d_{31}=\pm(0.12\pm0.06)$ $d_{16}=d_{21}=-d_{22}=\pm(2.0\pm0.25)$	1.06
KTP ($KTiOPO_4$)	$d_{15}=d_{31}=\pm(6.5\pm0.5)$ $d_{24}=d_{32}=\pm(5.0\pm0.5)$, $d_{33}=13.7$	1.06
quartz (SiO_2)	$d_{11}=0.36\pm0.05$	1.06
GaAs	$d_{14}=d_{25}=d_{36}=148\pm20$	10.6
Banana ($Ba_2NaNb_5O_{15}$)	$d_{31}=d_{32}=d_{15}=d_{24}=-13.2$, $d_{33}=-18.2$	1.06

If a field $E^{(1)}$ at the fundamental frequency ω_1 is incident on the crystal, a field $E^{(2)}$ at the second harmonic frequency $\omega_2=2\omega_1$ is generated at the expense of the fundamental wave. We consider the propagation in the z-direction only and transform the fields and the electric polarizations into the complex notation:

$$E^{(1)} = \frac{1}{2}\left(A^{(1)}\exp[i(\omega_1 t - k_1 z)] + CC\right) \tag{16.5}$$

$$P^{(1)} = \frac{1}{2}\left(P_c^{(1)} + P_c^{*(1)}\right) \tag{16.6}$$

The electric polarization P acts as a source for both fields $E^{(1)}$, which means that the propagation of each wave is described by the wave equation:

$$\frac{\delta^2 E^{(1)}}{\delta z^2} - \frac{1}{c_0^2}\frac{\delta^2 E^{(1)}}{\delta t^2} = -\frac{1}{\epsilon_0}\frac{\delta^2 P}{\delta t^2} \tag{16.7}$$

The electric polarization P is generated by the sum field $E^{(1)}+E^{(2)}$. After application of the SVE approximation (see Sec. 9.4), the amplitude $A^{(2)}$ of the second harmonic and the amplitude $A^{(1)}$ of the fundamental are given by:

$$2ik_1 \frac{\delta A^{(1)}}{\delta z} = \frac{\omega_1^2}{\epsilon_0 c_0^2} P_c^{(2)}(\omega_1)\exp[i(k_1 z - \omega_1 t)] \tag{16.8}$$

$$2ik_2 \frac{\delta A^{(2)}}{\delta z} = \frac{\omega_2^2}{\epsilon_0 c_0^2} P_c^{(2)}(\omega_2)\exp[i(k_2 z - \omega_2 t)] \tag{16.9}$$

where $P_c^{(2)}(\omega)$ denotes the component of $P_c^{(2)}$ that oscillates at the frequency ω. The meaning of these equations becomes clear if we insert the nonlinear polarization for a material with the nonzero nonlinear coefficient d_{11} (e.g. quartz). If the incident fundamental wave is linearly polarized in the x-direction, which means $A^{(1)}$ is given by $(A_x^{(1)},0,0)$, the second harmonic is also polarized in the x-direction. According to (16.4) and (16.6), the x-component of the second order polarization $P_c^{(2)}$ then reads:

$$P_{cx}^{(2)} = \frac{\epsilon_0}{2} d_{11}\,(A_x^{(1)}A_x^{*(1)} + A_x^{(2)}A_x^{*(2)} + A_x^{(1)}A_x^{(1)}\exp[2i(\omega_1 t - k_1 z)] +$$

$$+ 2A_x^{*(1)}A_x^{(2)}\exp[i(\omega_1 t - (k_2 - k_1)z)] + \ldots) \tag{16.10}$$

This is a simplified equation, assuming that the coefficient d_{11} is the same for each term. If we insert the terms oscillating at the frequencies ω_1 and $2\omega_1$ into (16.8) and (16.9), respectively, the following set of equations is obtained:

$$\frac{\delta A_x^{(1)}}{\delta z} = -i \frac{\omega_1^2 d_{11}}{2c_0^2 k_1} A_x^{*(1)} A_x^{(2)} \exp[-i\Delta kz] \tag{16.11}$$

$$\frac{\delta A_x^{(2)}}{\delta z} = -i \frac{\omega_2^2 d_{11}}{4c_0^2 k_2} A_x^{(1)} A_x^{(1)} \exp[i\Delta kz] \tag{16.12}$$

where $\Delta k = k_2 - 2k_1$. These equations reveal that the amplitude of the second harmonic can only increase significantly for $\Delta k = 0$. This condition is referred to as the *phase-matching condition*. If we consider the SHG as a transformation of two photons with energy $\hbar\omega_1$ into one photon with energy $\hbar\omega_2$, the phase-matching condition is equivalent to the conservation of the momentum:

$$\hbar k_1 + \hbar k_1 = \hbar k_2 \tag{16.13}$$

Since the wave number is related to the frequency and the speed of light via $k = \omega/c$, this relation means that the fundamental wave and the second harmonic must propagate with the same speed to avoid destructive interference of the second harmonic along the propagation direction (Fig. 16.1):

$$c(\omega_1) = \frac{c_0}{n(\omega_1)} = \frac{c_0}{n(2\omega_1)} = c(2\omega_1) \tag{16.14}$$

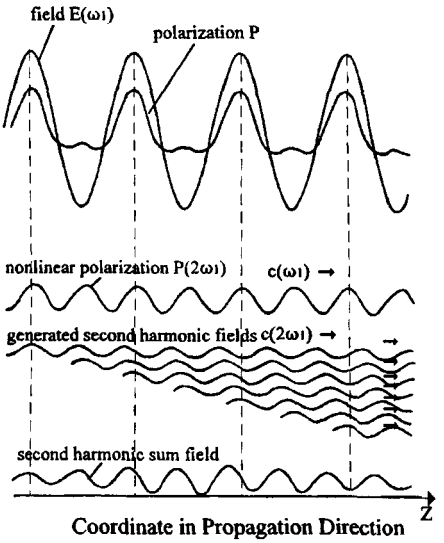

Fig. 16.1 Destructive interference of the second harmonic wave for $c(2\omega_1) < c(\omega_1)$.

For efficient SHG it is, therefore, necessary to match the indices of refraction n at the two frequencies. In isotropic crystals this condition can never be fulfilled because of normal dispersion ($n(2\omega_l)>n(\omega_l)$). In uniaxial crystals, phase matching can be achieved by letting the fundamental be an ordinary wave propagating at an angle θ to the optic axis of the crystal while the harmonic is propagating as an extraordinary wave in this direction , or vice versa (*Type I phase matching*). The refractive index n_e of the extraordinary wave is a function of the angle θ:

$$\frac{1}{n_e^2(\omega,\theta)} = \frac{\cos^2\theta}{n_o^2(\omega)} + \frac{\sin^2\theta}{n_e^2(\omega)} \tag{16.15}$$

where $n_o(\omega)$ is the index of refraction for the ordinary wave and $n_e(\omega)=n_e(\omega, \theta=\pi/2)$. The phase matching angle θ_p is defined by $n_o(\omega_l)=n_e(2\omega_l, \theta_p)$ for an ordinary fundamental wave and by $n_o(2\omega_l)=n_e(\omega_l, \theta_p)$ for an extraordinary fundame ntal wave. It is also possible to split the fundamental wave into an extraordinary wave and an ordinary wave to attain phase matching . This type of phase matching is referred to as *Type II phase matching*.

In general the fundamental wave and the second harmonic wave exhibit different polarizations and for intracavity SHG a polarizer has to be placed in the resonator to define the polarization of the fundamental wave. The reader may refer to [4.141] or [4.142] to get more insight into the physical aspects of phase matching and how it affects the differential equations (16.8) and (16.9). In the following we will assume the ideal case that the phase matching condition is met. The effect of a slight phase mismatch on the SHG efficiency shall be discussed later. Without lack of generality we use the scalar equations (16.11) and (16.12) with an effective nonlinear coefficient d_{eff} to discuss the conversion efficiency for SHG. The two equations can be solved analytically. For a nonlinear crystal with index of refraction n, the intensities I_1 and I_2 of the fundamental wave and the second harmonic wave, respectively, read as a function of the distance z in the crystal (Fig. 16.2):

$$I_2(z) = I_1(0)\,\tanh^2\left[\sqrt{\frac{d_{eff}^2}{n^3}\frac{\omega_1^2 I_1(0)}{2\epsilon_0 c_0^3}}\,z\right] = I_1(0)\,\tanh^2\left[\frac{z}{L}\right] \tag{16.16}$$

$$I_1(z) = I_1(0) - I_2(z) \tag{16.17}$$

where n is the index of refraction at both the fundamental and the second harmonic wavelengths. The conversion efficiency is defined as the fraction of the fundamental beam power that is converted into the second harmonic:

$$\eta_{SHG} = \frac{I_2(z)}{I_1(0)} = \tanh^2\left[\frac{z}{L}\right] \tag{16.18}$$

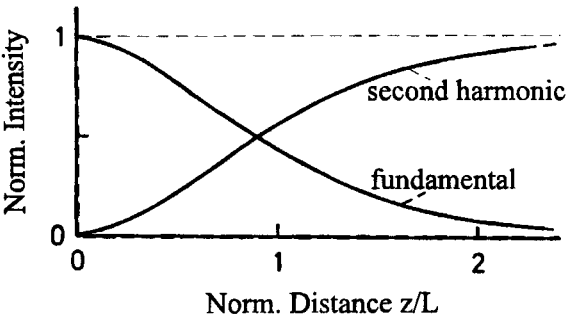

Fig. 16.2 Intensity of the second harmonic wave and of the fundamental wave as a function of the propagation distance z in the nonlinear crystal, according to (16.16) and (16.17).

At the characteristic distance $z=L$, 57% of the fundamental beam power has been converted into the second harmonic beam. For common nonlinear crystals an incident intensity of $I_1(0)=10^8\ W/cm^2$ results in a characteristic distance on the order of 10-20 mm. For low conversion efficiencies (<20%), Eq. (16.16) can be approximated by:

$$I_2(z) = I_1(0)\left[\frac{\omega_1^2}{2\epsilon_0 c_0^3} M\, I_1(0)\, z^2\right] \tag{16.19}$$

where M is the figure of merit of the crystal with (Table 16.2):

$$M = \frac{d_{eff}^2}{n^3} \tag{16.20}$$

The experimental values of the conversion efficiency are generally lower than predicted by (16.16) (Fig. 16.3). This is to be expected since we assumed a perfect crystal in which the phase matching condition is exactly met and a fundamental beam that exhibits a flat-top intensity profile. In reality the intensity is nonuniform and the conversion efficiency thus drops at the edges of the beam. Furthermore, due to the small spot size at the crystal the beam will have a small but finite divergence. For a 1.064μm Gaussian beam, a waist diameter of 0.5mm generates a half angle of divergence of 1.3mrad. For most crystals a deviation $\Delta\theta$ on the order of mrads from the phase matching angle θ_p will already decrease the conversion efficiency by 50%. Only the Fourier components of the fundamental beam that lie well within this acceptance angle will experience efficient conversion into the second harmonic. Other crystal properties that affect the conversion efficiency are the optical homogeneity, the absorption losses, and the temperature range within which the phase matching can be realized (typically ±1°C).

Table 16.2 Relative figure of merit M/M_{KDP} ($M_{KDP} = 0.027 x 10^{-24}\ m^2/V^2$), and the fundamental beam intensity $I_1(0)$ required to convert 57% of the fundamental power into the second harmonic for a crystal length of 10mm and a fundamental wavelength of 1.06μm, according to (16.16). The damage threshold represents the incident intensity at which surface damage occurs for a pulse duration of 15ns and a wavelength of 1.06μm (experimental data) [4.141,4.142].

Crystal (Phase Matching Type)	M/M_{KDP}	$I_1(0)$ [GW/cm^2]	Damage Threshold [GW/cm^2]
KDP (I)	1.0	5.642	14.4
KD*P (I)	1.0	5.642	0.5
ADP (I)	1.3	4.340	6.4
CDA (I)	1.7	4.,340	0.6
CD*A(I)	1.7	3.319	>0.3
LBO (I)	7.0	0.806	---
BBO (I)	25	0.226	23
LAP (I)	42	0.134	<13
$LiNbO_3$ (I)	105	0.054	0.05
KTP (II)	220	0.026	0.8
POM (I)	350	0.016	0.06
Banana (I)	570	0.010	<0.003

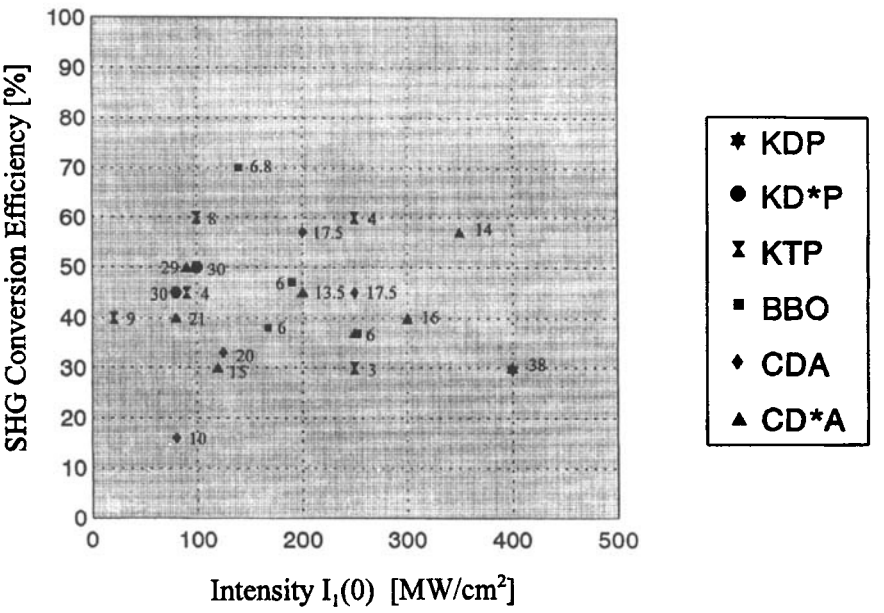

Fig. 16.3 Experimental values of the conversion efficiencies for external frequency doubling of Nd:YAG 1.064μm radiation versus the intensity of the fundamental wave at the nonlinear crystal [4.141,4.142]. The number at each data point is the crystal length in mm.

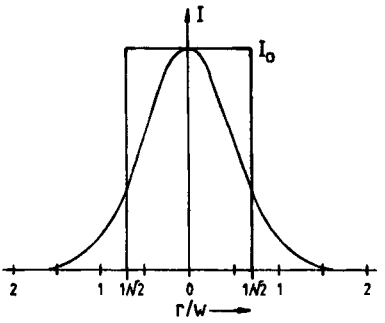

Fig. 16.4 A circular Gaussian beam with beam radius w has the sa me power content as a flat-top intensity profile with a radius of $w/\sqrt{2}$ and the same peak intensity I_0.

In most applications of SHG, a Gaussian beam at the fundamental wavelength is incident upon the nonlinear crystal. In order to apply the above discussed theoretical description, we have to approximate the Gaussian intensity profile by a flat top profile having the same power content. In circular symmetry, the power P_ω of the Gaussian beam with beam radius w and peak intensity I_0 is given by (Fig. 16.4):

$$P_\omega = I_0\, 2\pi \int_0^\infty \exp\left[-2\left(\frac{r}{w}\right)^2\right] r dr = I_0\, \pi \frac{w^2}{2} \tag{16.21}$$

Thus the radius of the flat-top profile is $w/\sqrt{2}$. For low conversion efficiencies, the intensity distribution of the second harmonic is also Gaussian. Neglecting the transverse spreading of the beam inside the crystal, we find with (16.19) that:

$$I_2(r) = \left[\frac{\omega_1^2 M z^2}{2\epsilon_0 c_0^3}\right] I_0^2 \exp\left[-4\left(\frac{r}{w}\right)^2\right] := B I_0^2 \exp\left[-4\left(\frac{r}{w}\right)^2\right] \tag{16.22}$$

The beam radius of the second harmonic wave is $\sqrt{2}$ times smaller than the beam radius of the fundamental wave. Both beams exhibit the same Rayleigh range and are, therefore, always in phase during propagation. The power of the second harmonic wave reads, according to (16.21) and (16.22):

$$P_{2\omega} = B I_0^2\, \pi \frac{w^2}{4} \tag{16.23}$$

Thus, the SHG conversion efficiency for a Gaussian fundamental beam is a factor of 2 lower compared to that of an incident beam with a flat-top intensity profile:

$$\eta_{SHG} = \frac{1}{2} B\, I_0 \tag{16.24}$$

This decrease is caused by the lower conversion efficiency at the outer areas of the beam. By increasing the fundamental beam intensity this influence of the mode structure becomes less pronounced since the wings of the beam are converted more efficiently. If we use the correct expression (16.16) for the conversion efficiency, the intensity distribution of the second harmonic field is not Gaussian anymore and the power reads:

$$P_{2\omega} = I_0\, 2\pi \int_0^{\infty} \exp\left[-2\left(\frac{r}{w}\right)^2\right] \tanh^2\left[\frac{z}{L}\exp\left(-\frac{r}{w}\right)\right] r\,dr \tag{16.25}$$

Compared to a flat-top input beam with intensity I_0, the SHG conversion efficiency is lower by a factor γ with:

$$\gamma = 2 \int_0^{\infty} \exp[-y^2] \tanh^2\left[\frac{z}{L}\exp\left(-\frac{y}{\sqrt{2}}\right)\right] y\,dy \Big/ \tanh^2\left[\frac{z}{L}\right] \tag{16.26}$$

The SHG conversion efficiency of a Gaussian fundamental beam thus reads:

$$\eta_{SHG} = \gamma \tanh^2\left[\frac{z}{L}\right] \tag{16.27}$$

For low fundamental beam intensities the factor γ is equal to 0.5 and it approaches unity for high conversion efficiencies. Figure 16.5 presents γ as a function of z/L.

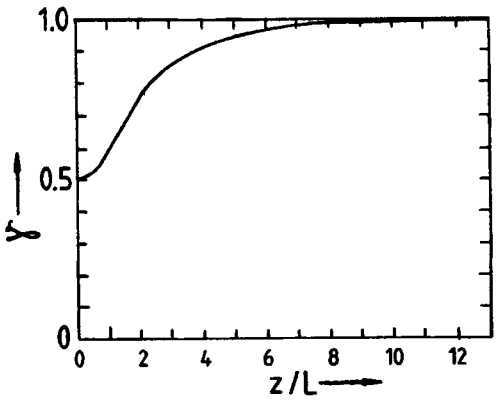

Fig. 15.5 Correction factor for Gaussian beam SHG according to (16.26).

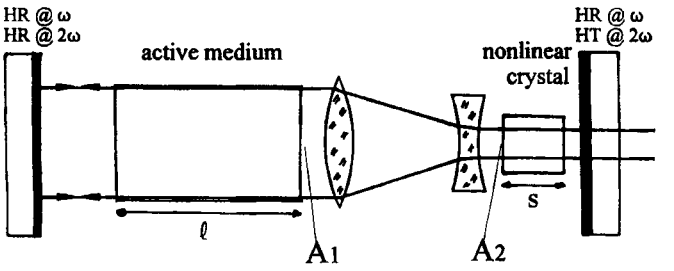

Fig. 16.6 Resonator model for Intracavity Second Harmonic Generation (ICSHG).

16.2.2 Efficiency of Intracavity Second Harmonic Generation

Since the intensity of the beam inside a laser resonator is much higher than the intensity of the laser output beam it is reasonable to place the nonlinear crystal inside the resonator to generate an output at the doubled frequency. Figure 16.6 depicts the resonator model we will use in the following to determine the laser efficiency at the second harmonic wave. The fundamental beam is generated by the laser medium and focused onto the nonlinear crystal to generate a high intensity. Both mirrors are highly reflecting for the fundamental wavelength and the right mirror transmits the second harmonic 100%. This means that the conversion efficiency of the nonlinear crystal acts as the output coupling loss of the resonator. If P_ω is the fundamental beam power incident on the nonlinear crystal and $P_{2\omega}$ is the power of the second harmonic wave generated, the effect of the nonlinear crystal on the fundamental beam can be described by a reflectance R with:

$$R = 1 - \frac{P_{2\omega}}{P_\omega} = 1 - \eta_{SHG} \tag{16.28}$$

where η_{SHG} is the conversion efficiency for the round trip. We can now calculate the average intensity I of the fundamental beam inside the active medium by using the steady-state condition for the round trip:

$$\exp\left[\frac{2g_0\ell}{1 + 2I/I_S} - 2\alpha_0\ell\right] = 1/R \tag{16.29}$$

where I_S is the saturation intensity, $g_0\ell$ is the small-signal gain and $\alpha_0\ell$ is the loss per transit. This expression can be written as:

$$\frac{2g_0\ell}{1 + 2I/I_S} = 2\alpha_0\ell + |\ln(1-\eta_{SHG})| \tag{16.30}$$

Note that the steady state condition (16.29) is only valid for a low small-signal gain and a high reflectance R because we neglect the z-dependence of the fundamental wave intensity inside the medium (see Section 10.1.1). This means that (16.30) is only applicable for low conversion efficiencies and, as a consequence, we cannot only replace the logarithmic term by η_{SHG} but also use (16.19) for its calculation. Equation (16.30) then becomes:

$$\frac{2\ g_0\ell}{1 + 2I/I_S} = 2\alpha_0\ell + 2BI \tag{16.31}$$

(16.32)

$$B = \frac{k\pi^2}{\epsilon_0 c_0}\ \gamma\ \frac{A_1}{A_2}\ \frac{M\ s^2}{\lambda_1^2} \qquad with\ k = \begin{bmatrix} 2\ for\ single\ pass\ SHG\ (see\ Fig.\ 16.6) \\ 4\ for\ dual\ pass\ SHG\ (see\ Fig.\ 16.10b) \end{bmatrix}$$

where A_1, A_2 is the cross-sectional area of the fundamental beam in the active medium and in the nonlinear crystal, respectively, s is the length of the nonlinear crystal, M its figure of merit, λ_1 is the fundamental wavelength, and γ is the correction factor according to (16.26) ($\gamma \approx 0.5$). After solving (16.31) for the intensity I the second harmonic output power can be determined with:

$$P_{2\omega} = A_1\ 2B\ I^2 \tag{16.33}$$

The final result reads:

$$P_{2\omega} = \frac{A_1}{8B}\left[\sqrt{(2\alpha_0\ell+BI_S)^2 + 8BI_S(g_0\ell-\alpha_0\ell)} - (2\alpha_0\ell+BI_S)\right]^2 \tag{16.34}$$

The second harmonic output power can be maximized by adjusting the parameter B of the nonlinear crystal. The optimum parameter B_{opt} is given by:

$$B_{opt} = \frac{2\alpha_0\ell}{I_S} \tag{16.35}$$

and the corresponding maximum output power reads:

$$P_{2\omega} = A_1\ I_S\ \alpha_0\ell\left[\sqrt{\frac{g_0\ell}{\alpha_0\ell}} - 1\right]^2 \tag{16.36}$$

A comparison with (10.13) indicates that this is exactly the output power we would achieve at the fundamental wavelength with optimum output coupling. In other words, if a laser resonator provides a maximum output power at the fundamental wavelength the same output power is provided at the second harmonic wavelength if the nonlinear crystal parameter B is optimized according to (16.35). This is, of course, only true if no additional losses occur due to absorption in the nonlinear crystal (typical loss coefficients are on the order of 0.01 per cm) and the active medium does not absorb the doubled frequency. Keep in mind that although all the fundamental beam power is converted into the second harmonic, the conversion efficiency of the nonlinear crystal may be extremely low. For a cw-laser that operates at an optimum output coupling of 5% for the fundamental wavelength, the conversion efficiency of the crystal in the optimized SHG resonator is also only 5%.

Example: Nd:YAG laser (λ_1=1.064μm, I_S=2kW/cm^2), rod diameter: 3mm (A_1= 7.1mm^2), rod length: 50mm, $g_0\ell$=0.4, $\alpha_0\ell$=0.02. To achieve optimum laser performance at the fundamental wavelength a mirror reflectance of $R=0.87$ is required (see (10.15)). According to (10.13), the corresponding maximum output power is 34W. Theoretically, this laser rod is capable of the same output power at the wavelength λ_2=0.532μm, provided that the nonlinear crystal is optimized according to (16.35). If we use LBO (see Table 16.2 for figure of merit M) and focus the intracavity beam to a diameter of 50 μm in the nonlinear crystal (A_1/A_2=3,600), Eqs. (16.32) and (16.34) yield an optimum crystal length of s = 21.2 mm for single pass and s=15 mm for double pass SHG.

For high gain or high output coupling, Eq. (16.29) cannot be used for the calculation of the second harmonic power. Instead, as was shown in Chapter 10, the differential equation (10.1) for the light amplification inside the active medium has to be solved using the boundary conditions at the resonator mirrors. In the case of ICSHG, however, it is not possible to find a simple analytical expression for the intracavity intensity I of the fundamental wave at the active medium since the mirror reflectance R is a function of the intracavity intensity. Furthermore, the correct expression (16.16) has to be used both for the mirror reflectance R and for the output power $P_{2\omega}$ of the second harmonic wave:

$$R = 1 - \tanh^2[\sqrt{2\,B\,I}] \tag{16.37}$$

$$P_{2\omega} = A_1\, I \tanh^2[\sqrt{2\,B\,I}] \tag{16.38}$$

Figure 16.7 presents the results of a numerical treatment of this problem. The maximum extraction efficiencies at the second harmonic wavelength are plotted versus the optimum crystal parameter B_{opt} for a saturation intensity of 2kW/cm^2. The maximum extraction efficiencies are the same as those shown in Fig. 10.4. As to be expected, expression (16.35) for the optimum crystal parameter represents a good approximation for low small-signal gains and low losses. The extraction efficiency as a function of the crystal parameter B is shown in Fig. 16.8 for different gains and losses. This graph provides the reader with a feeling for the allowed deviation of the crystal parameter from the optimum value.

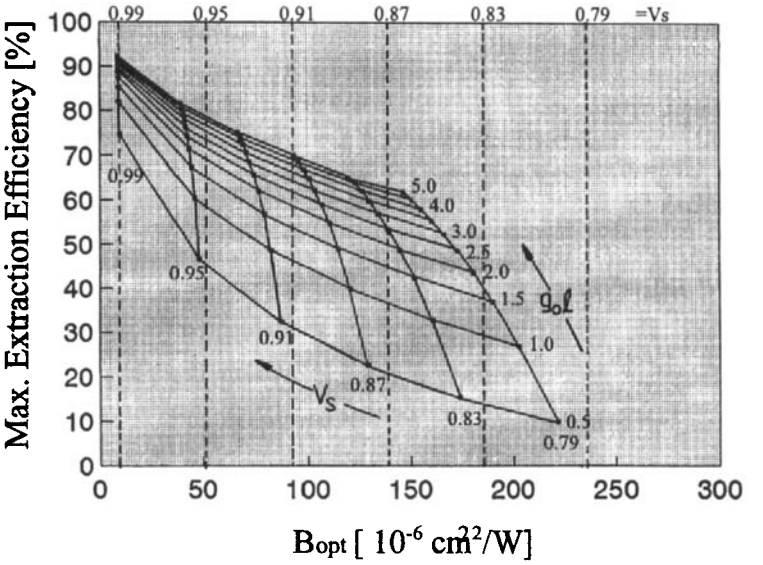

Fig. 16.7 Maximum extraction efficiencies versus the optimum crystal parameter B_{opt} for ICSHG (numerical calculation, I_S=2kW/cm^2). The curve parameters are the small-signal gain $g_0\ell$ and the loss factor per transit V_S=$exp[-\alpha_0\ell]$. The vertical lines represent B_{opt} calculated with (16.35). The extraction efficiency is the ratio of the output power at the second harmonic wavelength to the power P_{UL} available in the active medium in form of inversion with P_{UL}= $g_0\ell\ A_1\ I_S$(see also Chapter 10).

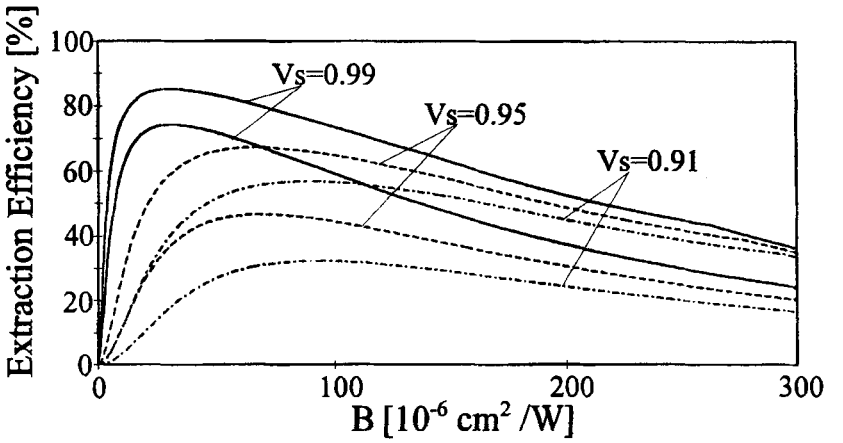

Fig. 16.8 Extraction efficiency as a function of the crystal parameter B. For each loss factor per transit V_S=$exp[-\alpha_0\ell]$, the upper and lower curve holds for a small-signal gain $g_0\ell$ of 1.5 and 0.5, respectively (I_S=2kW/cm^2).

16.2.3 Phase Mismatch, Longitudinal Modes, and Conversion Efficiency

Efficient second harmonic generation requires the fundamental and the second harmonic fields to be phase-matched, which means that both fields must exhibit the same phase velocity or index of refraction in the nonlinear crystal. The conversion efficiency is very sensitive to a phase mismatch Δkz between the two fields that occurs over a distance z inside the crystal. As long as the depletion of the fundamental field is low, the conversion efficiency for phase mismatched SHG is given by [4.141]:

$$\eta_{SHG} = \left[\frac{\omega_1^2}{2\epsilon_0 c_0^3} M I_1(0) z^2\right]\left[\frac{\sin(\Delta kz/2)}{\Delta kz/2}\right]^2 \tag{16.39}$$

with: $\Delta k = 2[n(\omega_1) - n(2\omega_1)]\omega_1/c_0$

For $\Delta k=0$ this expression is equivalent to (16.16). The mismatch of the wave vector can be caused by an angular deviation from the phase matching direction or by deviations in the temperature or in the fundamental wavelength since the indices of refraction are functions of all three parameters. For a crystal length of 10mm and a fundamental wavelength of 1.064μm, even a small refractive index difference of 0.0001 decreases the conversion efficiency by 26 %. Table 16.3 presents, for different nonlinear crystals, measured deviations in angle, temperature, and wavelength at which the SHG efficiency has dropped to one-half of the maximum value. When choosing a nonlinear crystal for ICSHG, these acceptance ranges are design parameters that are as important as the figure of merit M. It may even be advantageous to trade in the figure of merit for large acceptance ranges since the optimum crystal parameter B_{opt} can still be achieved by increasing the crystal length. Note in Table 16.3 that crystals for which a phase matching angle of 90° can be realized exhibit a high angular tolerance. In addition to slight phase mismatches, the output power at the second harmonic wavelength is also affected by the number m of longitudinal modes oscillating in the laser resonator. Assuming a statistical distribution of the phases of the axial modes, the conversion efficiency (16.39) for second harmonic generation as function of the number m of longitudinal modes reads:

$$\eta_{SHG}(m) = \frac{1}{2}\left[2-\frac{1}{m}\right]\left[\frac{\omega_1^2}{2\epsilon_0 c_0^3} M I_1(0) z^2\right]\left[\frac{\sin(\Delta kz/2)}{\Delta kz/2}\right]^2 = \frac{1}{2}\left[2-\frac{1}{m}\right]\eta_{SHG}(\infty) \tag{16.40}$$

In single mode operation, the conversion efficiency is reduced to half the maximum value. This means that in order to attain the maximum output power (16.36), the area of the fundamental beam in the nonlinear crystal has to be chosen to be half the area of the multimode case. An ICSHG resonator that has been optimized for single longitudinal mode operation, may therefore show a drop in the second harmonic output power if several modes start oscillating (resonator becomes overcoupled).

The major challenge in ICSHG is the realization of stable second harmonic emission with a low rms noise. Simultaneous oscillation of several longitudinal modes generates the so-called "green problem" [4.148,4.154], an amplitude instability due to longitudinal mode coupling caused by sum frequency generation of two different longitudinal modes. This chaotic amplitude fluctuation of the second harmonic can be suppressed by single-mode operation [4.155], by preventing the formation of standing waves in the resonator (unidirectional ring resonator [4.175], twisted mode resonator), by allowing two longitudinal modes that are orthogonally polarized (Fig. 16.9), or by using a high number m of longitudinal modes (long resonator) [4.153]. In [4.174] an rms stability of better than 0.1% was reported for a diode pumped Nd:YVO_4/LBO system with on the order of 100 axial modes. In recent years, quiet second harmonic multimode operation has also been reported for longitudinal mode numbers below 30, in some cases as low as 3. At present, there is no satisfactory explanation why quiet ICSHG operation can occur for a low number of longitudinal modes.

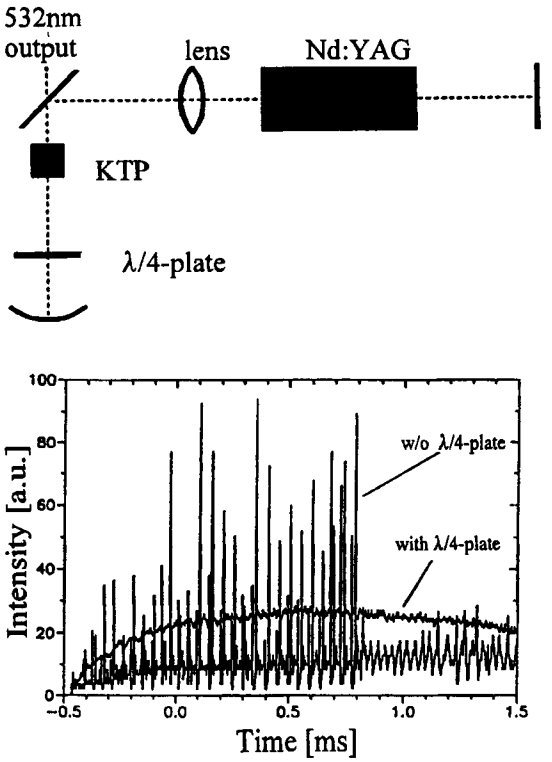

Fig. 16.9 Measured second harmonic intensity of a pulsed, flashlamp pumped Nd:YAG laser with ICSHG in type II KTP. By inserting a quarter-wave plate, whose principal axes are rotated by 45° with respect to the axes of the KTP, sum frequency generation of different longitudinal modes is suppressed, resulting in considerably reduced rms noise [S.31].

Table 16.3 Experimental values of the phase matching angle and the angular, spectral, and temperature deviations at which the SHG conversion efficiency has dropped by 50% (λ_1=1.064μm, crystal length s=10mm) [4.141,4.142].

Crystal (Phase matching type)	θ_P [degree]	Δθ [mrad]	ΔT[°C]	Δλ [nm]
KDP (I)	41	2.7	11	5.6
KDP(II)	59	5.3	13.2	7.3
KD*P (II)	53.5	5.0	6.7	5.6
CDA (I)	84	12.3	2	-
CDA (I)	90	69	5.8	-
CD*A (I)	79.3	7.2	3.3-6.4	2.45
Banana (II)	76	5.4	0.5	-
Banana (I)	90	43	0.5	-
KTP (II)	25	15-68	25	0.56
KTP (I)	90	15	25	0.56
BBO (I)	23	1.5	55	-
LBO (I)	90	52	4	-

16.2.4 Resonator Configurations

In order to realize the optimum crystal parameter B_{opt} given by (16.32) and (16.35) we can play with three parameters: the crystal length s, the figure of merit M, and the ratio of the cross sectional areas A_1/A_2. However, the ranges of the first two parameters are more or less limited and the conversion efficiency has to be optimized by utilizing a resonator configuration that provides a high ratio A_1/A_2 . Since we have to limit the angle of divergence of the fundamental beam, we are particularly interested in stable resonators that exhibit a large Gaussian beam diameter at one resonator mirror, where the active medium is placed, and have a small beam waist at the location of the nonlinear crystal. If mirror 1 is the resonator mirror at which the active medium is to be placed, there are two regions in the stability diagram where these Gaussian beam properties can be attained; near the stability limit $g_1g_2=1$ with $g_2<-1$ (concentric resonators) and near the axes $g_1=0$ with $g_2<1$.

Resonators in the latter region exhibit an effective length which is equal or slightly shorter than the radius of curvature of mirror 1 (Fig. 16.10a). If a concave mirror 2 with a relatively large radius of curvature is used, the beam waist is slightly shifted inwards and the nonlinear crystal can be placed close to this mirror. In solid state lasers that are end-pumped with laser diodes with output powers in the Watt range, the active medium is also placed at this side since the diode beam has to be tightly focused in order to reach laser threshold, resulting in a high fundamental beam power (Fig. 16.11).

In concentric resonators, the centers of curvatures of both concave mirrors are on top of each other and this point is the location of the beam waist. The active medium is placed close to the mirror with the larger radius of curvature. Fig. 16.10b presents a resonator that is equivalent to a concentric resonator (see also Fig. 16.12).

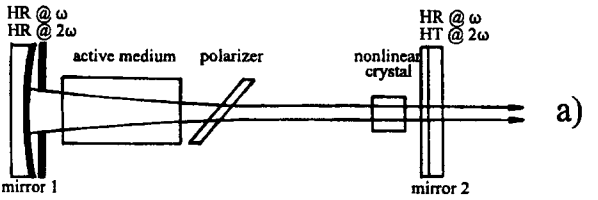

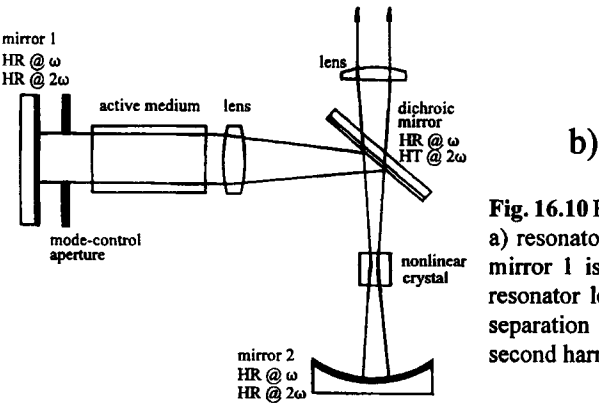

Fig. 16.10 Resonator configurations for ICSHG. a) resonator near the axis $g_i=0$. The radius of mirror 1 is slightly shorter than the effective resonator length. b) concentric resonator with separation of the fundamental field and the second harmonic field by a dichroic mirror.

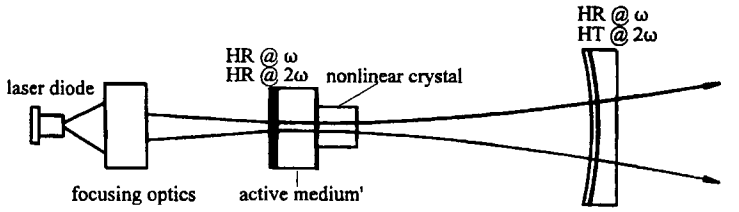

Fig. 16.11 Second harmonic generation in a diode pumped solid state laser.

Note that the combination of the flat mirror and the focusing lens exhibits the same imaging properties as a concave mirror but provides a higher fill factor in the active medium. The use of the dichroic beamsplitter prevents the second harmonic field from entering the active medium and being partially absorbed. Since the second harmonic generation occurs in both propagation directions, the fundamental field and the second harmonic field must be in phase at both endfaces of the nonlinear crystal. Due to the dispersion of air, the propagation from the crystal to mirror 2 and back generates a phase shift between the two fields which, depending on the propagation distance and the phase shift induced by the HR mirror, may lead to destructive interference of the second harmonic. This phase shift of 27.4° per cm of propagation distance has to be compensated by slightly translating mirror 1 until the second harmonic power is maximized [4.146].

Experimental examples of ICSHG in neodymium doped YAG and Vanadate lasers are presented in Figs. 16.12 to 16.14. These three systems represent the state of the art of second harmonic generation for diode pumped and flashlamp pumped Nd:YAG lasers. An overview of the performance of solid state lasers with ICSHG is given in Table 16.4. In general, the second harmonic power can be as high as η=60-70% with respect to the power attained when the laser is operated at the fundamental wavelength (with optimum output coupling). In some instances, conversion efficiencies as high as 90% have been reported.

Table 16.4 Intracavity SHG of different solid state lasers. $P_{2\omega}$ is the power at the second harmonic wavelength, η is the ratio of $P_{2\omega}$ to the power achieved at the fundamental wavelength, P_{electr} is the electrical pump power to the flashlamps, and P_{opt} is the optical power incident on the active medium.

Material	λ_2[nm]	crystal	mode of operation	η[%]	$P_{2\omega}$	Ref.
Nd:YAG	532	KTP	cw-flashlamp, P_{electr}=4.9kW	-	25W	[4.162]
Nd:YAG	532	KTP	cw-flashlamp, Q-switch, P_{electr}=4kW	53	21.5W	[4.152]
Nd:YAG	532	KTP	cw-flashlamp, Q-switch, P_{electr}=8.5kW	21	53W	[S.17]
Nd:YAG	532	KTP	cw-flashlamp, Q-switch, P_{electr}=8kW	-	97W	[4.161]
Nd:YAG	532	KTP	cw-laser diode, Q-switch, P_{opt}=2.2W	50	340mW	[4.157]
Nd:YAG	532	KTP	cw-laser diode, P_{opt}=11W	48	1.05W	[4.163]
Nd:YAG	532	KTP	cw-laser diode, P_{opt}=15.3W	-	3.5W	[4.166]
Nd:YAG	532	KTP	cw-laser diode, P_{opt}=14W	-	3.1W	[4.175]
Nd:YAG	532	KTP	cw-laser diode, modelocked, P_{opt}=55W	56.6	3.0W	[4.158]
Nd:YAG	532	LBO	cw-laser diode, Q-switch, P_{opt}=19W	84	3.2W	[4.188]
Nd:YAG	532	LBO	cw-laser diode, Q-switch, P_{opt}=40W	67	4W	[4.167]
Nd:YAG	532	LBO	cw-laser diode, Q-switch, P_{opt}=800W	90	138W	[4.184]
Nd:YAG	473	$KnbO_3$	cw-laser diode, P_{opt}=279mW	9.5	43mW	[4.173]
Nd:YAG	473	LBO	cw-laser diode, P_{opt}=22.7W	39.4	1.3W	[4.182]
Nd:YAG	473	BiBO	cw-laser diode, P_{opt}=21W	61	2.8W	[4.190]
Nd:YVO_4	532	KTP	cw-laser diode, P_{opt}=900mW	27.6	105mW	[4.171]
Nd:YVO_4	532	KTP	cw-laser diode, P_{opt}=1.2W	-	250mW	[4.185]
Nd:YVO_4	532	KTP	cw-laser diode, P_{opt}=4W	-	1.05W	[4.172]
Nd:YVO_4	532	KTP	cw-laser diode, P_{opt}=12.6W	46	3.2W	[4.179]
Nd:YVO_4	532	LBO	cw-laser diode, P_{opt}=19.5W	65	6.1W	[4.174]
Nd:YVO_4	532	LBO	cw-laser diode, P_{opt}=20W	-	8.5W	[S.18]
Nd:YVO_4	532	LBO	cw-laser diode, P_{opt}=30W	-	8.9W	[4.187]
Nd:YLF	523.5	LBO	cw-laser diode, P_{opt}=10W	24	0.9W	[4.164]
Nd:LSB	531	KTP	cw-laser diode, P_{opt}=2.05W	55	522mW	[4.165]
Nd:LiLuF	455	LBO	cw-laser diode, P_{opt}=1.8W	5.7	42mW	[4.186]
Cr:LiSAF	428-444	$KnbO_3$	cw-laser diode, P_{opt}=680mW	6.8	13mW	[4.170]
Cr^{4+}:forsterite	613-655	PPLN	cw-1064nm YAG, P_{opt}=6.8W	18.4	45mW	[4.189]

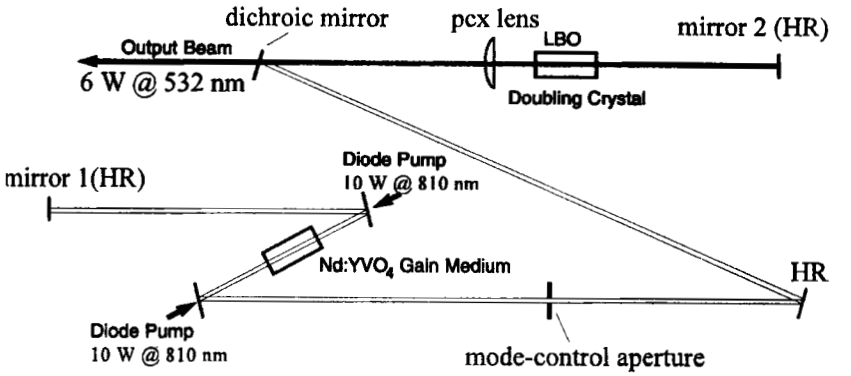

Fig. 16.12 ICSHG in a diode pumped Nd:YVO_4 laser. The LBO crystal is held at a temperature of 150°C to achieve non-critical phase matching (Type I). The maximum second harmonic output power is 6.1W at an optical pump power from the laser diodes of 20 W. The resonator length is 1m, allowing a large number of axial modes (~100) to oscillate. The axial multimode operation results in a high stability and a low RMS noise (<0.04%). Without frequency doubling, the output power at the fundamental wavelength is 9.4W [4.174] (Millennia V, courtesy of Spectra-Physics, Mountain View, CA, 1996). A shorter version of this resonator, released in 2000, provides green output powers in excess of 12W at about twice the pump power (Millennia X).

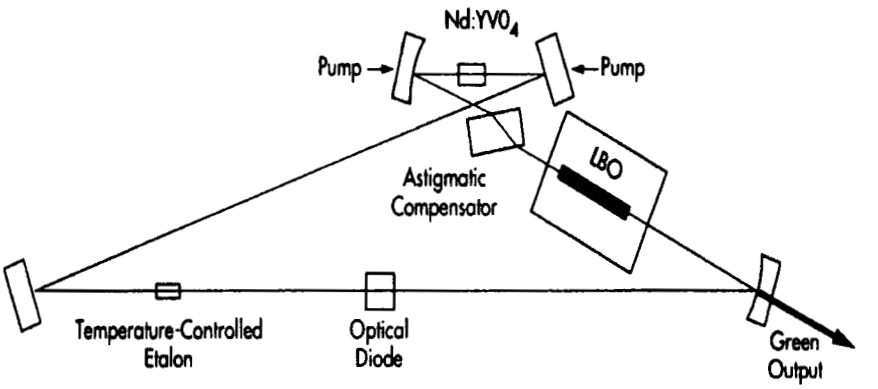

Fig. 16.13 ICSHG in a diode-pumped Nd:YVO_4 ring laser. An output power at 532nm in excess of 18W is obtained in single mode operation with an rms noise of less than 0.03% (18W Verdi, courtesy of Coherent,Santa Clara, CA, 2004).

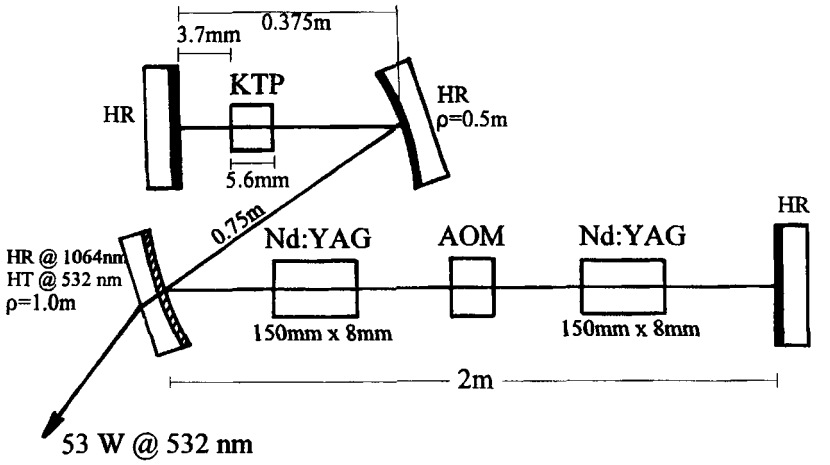

Fig. 16.14 Cw flashlamp pumped Nd:YAG laser with ICSHG providing a maximum average output power of 53 W at the second harmonic wavelength of 532nm for an electrical pump power of 8.5kW (4.25 kW per rod). Pulse duration: 500ns, pulse repetition rate: 5kHz; AOM: acousto-optic modulator [S.17] (courtesy of Laser- und Medizin Technologie Berlin gGmbH, Berlin, Germany).

16.3 Intracavity Third Harmonic Generation

16.3.1 General Properties of Third Harmonic Generation

In general, tripling the frequency of the fundamental wave can be accomplished directly by a one step, third order nonlinear process, in which three fundamental photons are combined into one photon with three times the energy. However, the nonlinear coefficients for this direct process are relatively small, resulting in very low conversion efficiencies in the sub-percent range for typical fundamental beam intensities of hundreds of MW per cm^2. A more efficient way to generated the tripled frequency is the doubling of a portion of the fundamental and subsequent sum frequency generation (SFG) of the two resulting fields (Fig. 16.15). This process is mainly used for frequency tripling of pulsed infrared solid state lasers [4.191-4.193, 4.203-4.205]. In order to achieve 100% conversion efficiency, 67% of the fundamental power has to be converted to the second harmonic since this results in an equal number of fundamental and second harmonic photons in the SFG crystal. Figure 16.16 shows calculated conversion efficiencies as a function of the total input intensity on the SFG crystal (type II KDP, 1064nm fundamental) for different ratios M of second harmonic to fundamental power, assuming a flat-top in intensity profile. A mismatch of green and infrared photon numbers will result in back-conversion and complete suppression of the third harmonic at certain input intensities. However, with matched photon numbers, it is possible to attain 100% conversion efficiency.

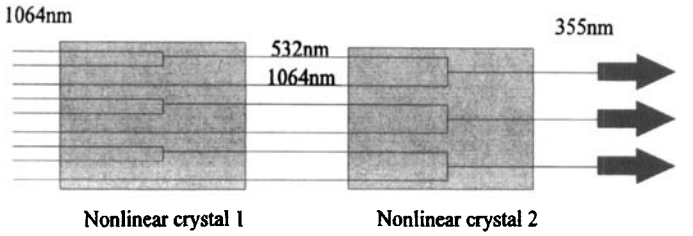

Fig. 16.15 Third harmonic generation via sum frequency generation of the fundamental and the doubled wavelength. 100% conversion occurs, if 67% of the fundamental power is converted into the second harmonic in the doubling crystal.

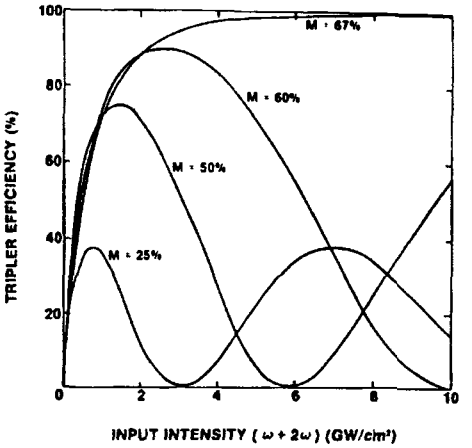

Fig.16.16 Tripling efficiency of a 9mm thick phase-matched KDP type II crystal as a function of the total input intensity for various percentages M of second harmonic power content in the input [4.191] (© Optics Communications, 1980).

The presented calculations are numerical solutions to two sets of differential equations, one describing the doubling process, and the subsequent one for sum frequency generation. In both equations flat-top intensity distributions both in space and time are assumed [4.191]. Assuming perfect phase matching and no losses, the equations for the doubling process read:

$$\frac{\delta A_1}{\delta z} = -i \frac{\pi d_2}{n_2 \lambda} A_1^* A_2 \tag{16.41}$$

$$\frac{\delta A_2}{\delta z} = -i \frac{\pi d_2}{n_2 \lambda} A_1^* A_1 \tag{16.42}$$

where d_2 is the effective nonlinear coefficient for SHG, n_2 is the refractive index of the crystal and λ is the fundamental wavelength. The fundamental field A_1 and the second harmonic field A_2 at the end of the SHG crystal serve as input fields for the second set of equations describing the sum frequency generation:

$$\frac{\delta A_1}{\delta z} = -i \frac{\pi d_3}{n_3 \lambda} A_2^* A_3 \tag{16.43}$$

$$\frac{\delta A_2}{\delta z} = -2i \frac{\pi d_3}{n_3 \lambda} A_1^* A_3 \tag{16.44}$$

$$\frac{\delta A_3}{\delta z} = -3i \frac{\pi d_3}{n_3 \lambda} A_1 A_2 \tag{16.45}$$

where d_3 is the effective nonlinear coefficient for SFG (see Table 16.5), n_3 is the refractive index of the crystal and A_3 is the field of the third harmonic. The differential equations (16.41-16.45) can also be used to generate a numerical model that simulate third harmonic generation for more realistic beams that include focusing as well as a transverse and temporal intensity distribution. In practice, most frequency-tripled solid state lasers are Q-switched or mode-locked Nd:YAG or Nd:YVO_4 lasers in fundamental mode operation, exhibiting output pulses with near-Gaussian temporal pulse shapes. In this case, matching the fundamental and the second harmonic photon numbers can only be partially realized, resulting in tripling conversion efficiencies that remain well below 100% .

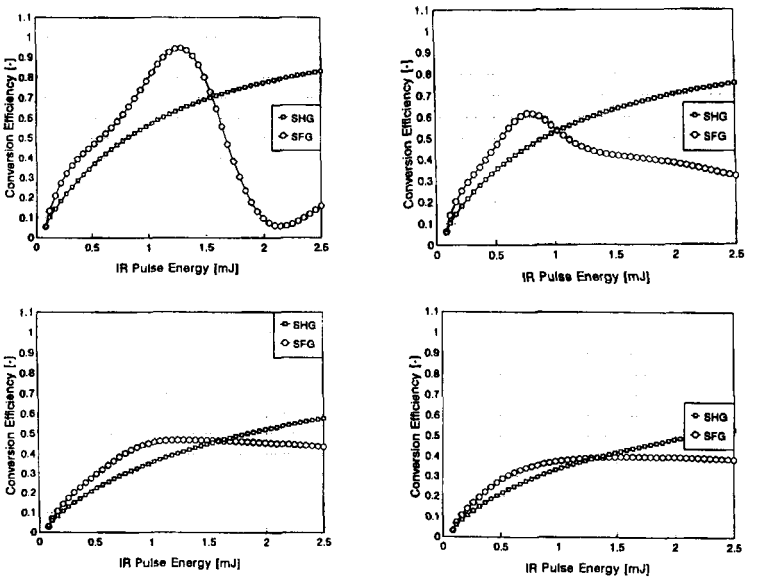

Fig. 16.17 Calculated conversion efficiencies in the SHG crystal (20mm long LBO type I, d_2=0.83pm/V) and the SFG crystal (20mm long LBO type II, d_3=0.66 pm/V) as a function of the total input energy at 1064nm for different spatial and temporal intensity distributions. a) flat-top in spce in time, b) flat-top in space, Gaussian in time, c) Gaussian in space, flat-top in time, d) Gaussian in space and time. Pulse duration: 50ns, IR beam diameter in SHG crystal: 140 μm, IR beam diameter in SFG crystal: 70 μm. Equations (16.41-45) were solved numerically.

While the beam center may exhibit the perfect balance of IR and green photons, the wings of the pulse will experience a much lower conversion efficiency. Increasing the input intensity does not necessarily lead to an enhancement of the over efficiency, because the increased conversion in the wings of the pulse is off-set by a decreased conversion in the beam center. This may result in an intensity dip in the center of the UV beam. An example is shown in Fig. 16.17, in which calculated IR to UV conversion efficiencies are shown for 50ns long input pulses at 1064nm using type I LBO and type II LBO, the crystals most commonly used for third harmonic generation [4.195,4.198,4.203], as the SHG and SFG crystal, respectively. For an intensity profile that is flat-top in time and space, a maximum UV conversion of close to 100% is obtained at a pulse energy at which the doubling efficiency is 67%. Introducing a Gaussian intensity distribution in time or space leads to a substantial decrease of the maximum conversion efficiency. For a Gaussian beam with Gaussian-shaped temporal pulses, the maximum tripling efficiency that can be attained is about 43%, with a similar value for the doubling efficiency.

However, this maximum possible conversion efficiency can only be obtained for a perfect spatial and temporal overlap between the fundamental and the second harmonic intensities. Inside commonly used SFG crystals, the two beams will propagate at a slight angle, referred to as the walk-off angle. This results in a decreased effective interaction length inside the crystal. If the walk-off angle is not too large, walk-off compensation schemes like the one shown in Fig.16.18 can be applied to improve the tripling efficiency [4.196,4.199]. Measured IR to UV conversion efficiencies of up to 40% have been reported for extra-cavity frequency tripled Nd:YVO_4 lasers with walk-off compensation [4.125, 4.203].

The choice of the SFG crystal is a balance of finding a high nonlinear coefficient and a large acceptance angle, combined with a small walk-off angle (Table 16.5). At present, the majority of ultraviolet solid state lasers use LBO as the type II SFG crystal, because the relatively large acceptance angle allows spot sizes of the fundamental beam of 100 microns or less inside the crystal. In addition, the relatively small walk-off angle makes compensation schemes easier to implement.

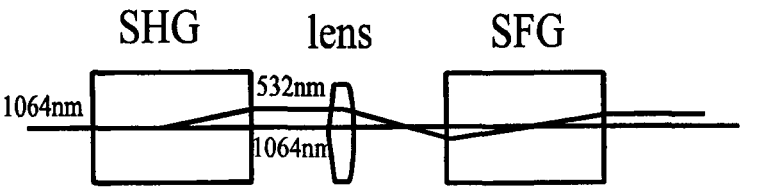

Fig. 16.18 Walk-off compensation scheme, using a focusing lens to cross the IR and the green beam near the center of the SFG crystal. In order for this scheme to work, the two beams need to be slightly separated in front of the lens. In this case, the walk-off in the SHG crystal is used to generate the separation.

Table 16.5 Nonlinear coefficients, acceptance angles and walk-off angles of different nonlinear crystals for 355nm generation via sum frequency generation (1064nm + 532nm) [4.208]

crystal	nonlinear coefficient d_3 [pm/V]	acceptance angle x length [mrad cm]	walk-off angle [mrad]
LBO, type II	0.66	5.0	9.3
type I	0.90	---	18.3
CLBO, type II	0.93	1.2	37.3
type I	0.62	0.8	37.1
CBO, type II	1.15	----	16.2
type I	0.91	1.9	17.5
BBO, type II	1.2	0.6	77.7
type I	1.72	0.4	72.1

Figure 16.19 depicts calculated IR to UV conversion efficiencies (1064nm to 355nm) for extra-cavity third harmonic generation as a function of the beam diameter in the type II LBO SFG crystal for a Gaussian beam with 20kW peak power. Parameter of the curves is the beam diameter in the doubling crystal (non-critically phase matched type I LBO). A plane-wave approximation is used (no beam spreading due to diffraction) and walk-off is not included in the numerical model. This graph indicates that for Q-switched or modelocked IR lasers, which typically exhibit peak powers between 5 and 50 kW, spot diameters on the order of 100-200 μm are required in both crystals to attain the maximum conversion efficiency of about 43%.

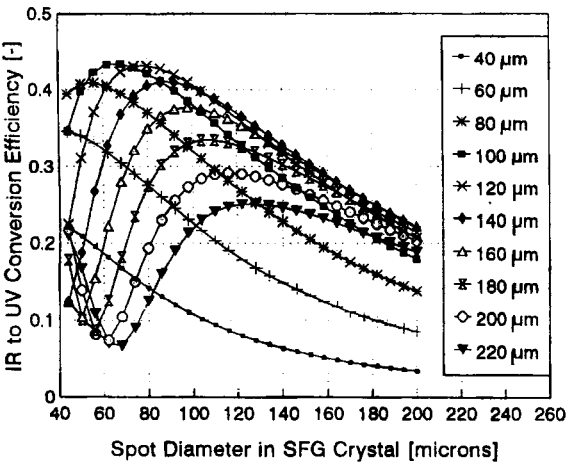

Fig. 16.19 Calculated 1064nm to 355nm conversion efficiency for a Gaussian beam with 1mJ pulse energy and 50ns pulse duration (Gaussian pulse, $1/e^2$ full width) as a function of the 1064nm beam diameter in the SFG crystal (20mm long type II LBO, d_3=0.66 pm/V). Curve parameter is the 1064nm beam diameter in the doubler cyrstal (20mm long LBO, d_2=0.83 pm/V). Equations (16.41)-(16.45) were applied to each of 100 x 100 points in time and space, using a Gaussian input field distribution. No walk-off included in the model.

16.3.2 Properties of Intracavity Third Harmonic Generation

Similar to intracavity second harmonic generation, the two nonlinear crystals can be placed inside the resonator to make use of the high intra-cavity intensity of the fundamental. The major advantage of this technique is that, compared to the extra-cavity arrangement, the beam diameters in the nonlinear crystals can be increased considerably, typically by a factor of five for Q-switched systems. As a result, it is not necessary to use walk-off compensation schemes to attain high conversion efficiencies since the walk off (typically 50-100 microns) is one order of magnitude smaller than the beam size. Lifetime of the SFG crystal is also enhanced due to the lower UV power density. In addition, the pulse-to-pulse stability is improved since resonator output coupling is a function of the fundamental beam intensity. Similar to a standard resonator, a change in output coupling generates only small changes in output power if the resonator is operated near the optimum output coupling. Thus, a variation of the fundamental beam intensity, due to pump power variations or Q-switch jitter, has a much lower effect on the UV output as compared to extra-cavity systems. A typical Q-switched infrared solid state laser resonator with intracavity third harmonic generation is shown in Fig. 16.20. An intra-cavity beam splitter and a prism are used to extract and separate the residual green and the UV beam. Alternative output coupling techniques include transmission through one of the infrared HR mirrors [4.202,4.205], and wavelength separation using intracavity prisms [4.202] or a Brewster-cut SFG crystal [4.200].

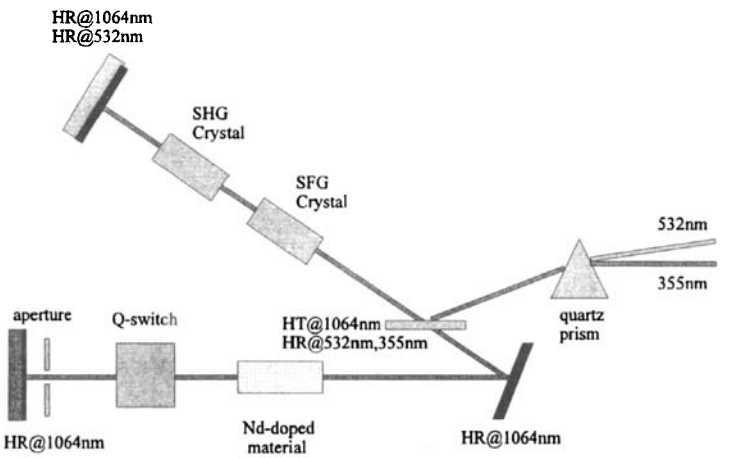

Fig. 16.20 Schematic of a Q-switched solid state laser with intracavity harmonic generation (after [4.210]). The resonator for the fundamental wavelength is formed by the three 1064nm HR mirrors (marked in black). After a double pass through the SHG crystal, the generated green power is mixed with the fundamental in the SFG crystal. Output coupling of the resonator is provided by the nonlinear conversion to the green and the UV.

In an ideal arrangement, the green power is completely depleted in the SFG crystal and the third harmonic power is equal to the power the resonator would provide at the fundamental wavelength with optimum output coupling (see Sec.16.2.2). For flat-intensity profiles, this can be accomplished by properly choosing the fundamental beam diameters in the nonlinear crystals as well as optimizing the crystal lengths. Let us use a simplified model to understand the key issues of this optimization. After the dual pass in the SHG crystal, the green power is given by:

$$P_G = \eta_{SHG} P_{IR} \tag{16.46}$$

where P_{IR} is the fundamental power entering the SHG crystal and η_{SHG} is the dual pass conversion efficiency. If we assume that the green power is completely depleted in the SFG crystal, the third harmonic power must be given by (remember that each green photon is added to an infrared photon with half the energy!):

$$P_{UV} = \frac{3}{2} \eta_{SHG} P_{IR} \tag{16.47}$$

The combination of the two nonlinear crystals acts as an output coupler for the fundamental wavelength resonator with a reflectivity:

$$R = \frac{P_{IR} - P_{UV}}{P_{IR}} = 1 - \frac{3}{2} \eta_{SHG} \tag{16.48}$$

Maximum UV power is obtained if the reflectivity R is equal to the optimum reflectivity of the resonator when operated at the fundamental wavelength (see Eq. (10.15)). The optimum SHG efficiency is thus given by:

$$\eta_{SHG,opt} = \frac{2}{3} \left[1 - R_{opt}\right] \tag{16.49}$$

Typically, solid state lasers in Q-switched operation exhibit optimum reflectivities between 50% and 90%, which translates into optimum SHG efficiencies between 33% and 7%. Therefore, optimized intracavity third harmonic generation requires considerably lower green conversion than the 67% needed in the extra-cavity scheme. Once the optimum conversion is realized by choosing the correct beam size and SHG crystal length, the SFG conversion efficiency can be maximized separately by changing the focusing into the SFG crystal and the crystal length. Theoretically, this results in a third harmonic power that is equal to the maximum output power at the fundamental wavelength. A calculated example for a Q-switched, diode pumped Nd:YVO_4 laser is shown in Fig.16.21. Graph a) shows the performance for beam diameters in the nonlinear crystals that are close to optimal. At a repetition rate of 23kHz, 30W of 355nm power is obtained with 22% IR to green conversion and 1W of residual green power.

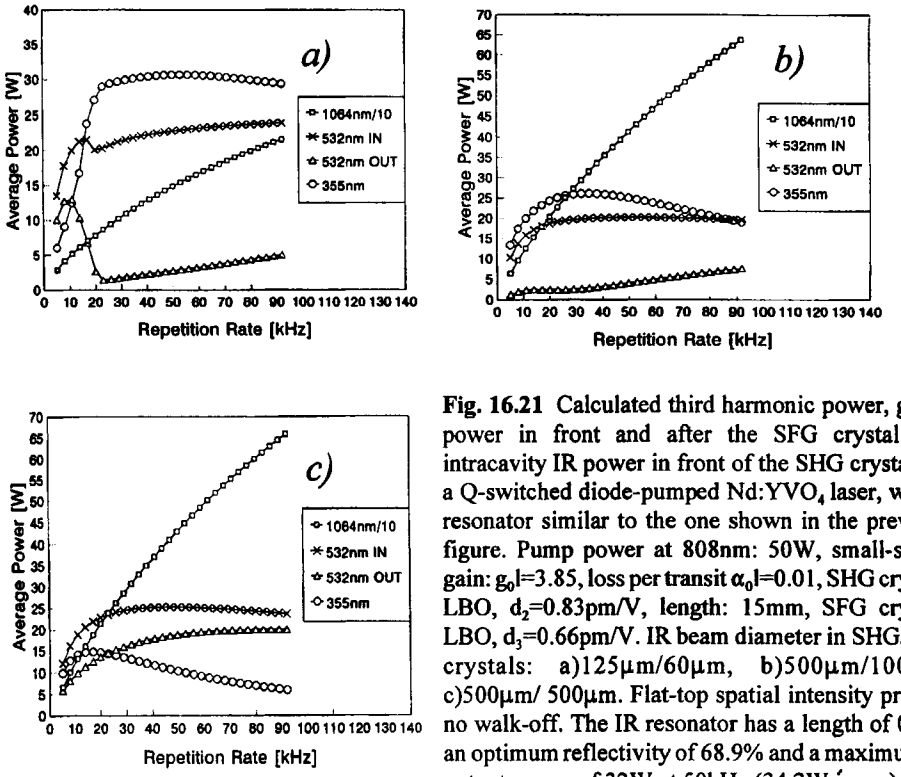

Fig. 16.21 Calculated third harmonic power, green power in front and after the SFG crystal and intracavity IR power in front of the SHG crystal for a Q-switched diode-pumped Nd:YVO_4 laser, with a resonator similar to the one shown in the previous figure. Pump power at 808nm: 50W, small-signal gain: $g_0 l$=3.85, loss per transit $\alpha_0 l$=0.01, SHG crystal: LBO, d_2=0.83pm/V, length: 15mm, SFG crystal: LBO, d_3=0.66pm/V. IR beam diameter in SHG/SFG crystals: a)125μm/60μm, b)500μm/100μm, c)500μm/ 500μm. Flat-top spatial intensity profile, no walk-off. The IR resonator has a length of 0.5m, an optimum reflectivity of 68.9% and a maximum IR output power of 32W at 50kHz (34.2W in cw).

According to (16.49) and (10.15), the optimum green conversion for this laser is about 21%, and the maximum IR power at 23kHz would be 31W. This example clearly indicates, that in order to maximize the UV power, the beam diameters inside the crystals have to be chosen similar to those used in extra-cavity sum frequency generation. This is easy to understand because for an optimum output coupling of 50%, the intracavity IR power is only twice as high as the extra-cavity power. For common nonlinear crystals, the major advantages of intracavity third harmonic generation, i.e. increased crystal lifetime and insensitivity to walk-off, cannot be realized when the resonator is designed for maximum third harmonic power. For this reason, commercial intracavity third harmonic lasers are under-coupled with beam diameters inside the nonlinear crystals that are several times larger than the ones providing optimum coupling (see Fig. 16.21c). This results in IR to UV efficiencies that are close to the extra-cavity case (up to 50%), but with improved pulse-to-pulse stability, especially at high repetition rates (>100kHz). However, despite this superior performance, intracavity third harmonic generation is less common in solid state UV lasers, because of technical problems that are generated by the coupling of the fundamental and the harmonic intensities and the degradation of optical components due to UV irradiation.

16.4 Resonators with Phase-Conjugate Mirrors

16.4.1 General Properties of a Phase-Conjugate Mirror

Compared to a conventional mirror, the imaging properties of a phase conjugating mirror are quite different [4.232,4.242]. Whereas a conventional mirror reflects light rays according to the reflection law of geometrical optics, rays hitting a phase-conjugate mirror (PCM) are simply reversed, independent of the angle of incidence (Fig. 16.22a). If a spherical wave is incident on the PCM, with:

$$E(r,t) = \frac{E_0}{r} \exp[-i\omega t] \exp[i(kr+\phi)] \tag{16.50}$$

where r is the distance from the origin and ϕ is an arbitrary phase shift, the reflected wave converges back into its origin:

$$E_{ref}(r,t) = C \frac{E_0}{r} \exp[-i\omega t] \exp[-i(kr+\phi)] \tag{16.51}$$

where C is the amplitude reflectance of the PCM. The term phase conjugation now becomes obvious since the reflected wave is obtained by replacing the spatial phase term with its complex conjugate. If a plane wave experiences a phase distortion ϕ by passing through a medium, the PCM exactly reverses the phase and after the second transit through the medium the plane wave front is restored (Fig. 16.22b). Thus we can use a PCM to compensate the phase distortions induced by the active medium. The main application of PCMs is the compensation of thermal lensing in solid state laser materials (Fig. 16.23).

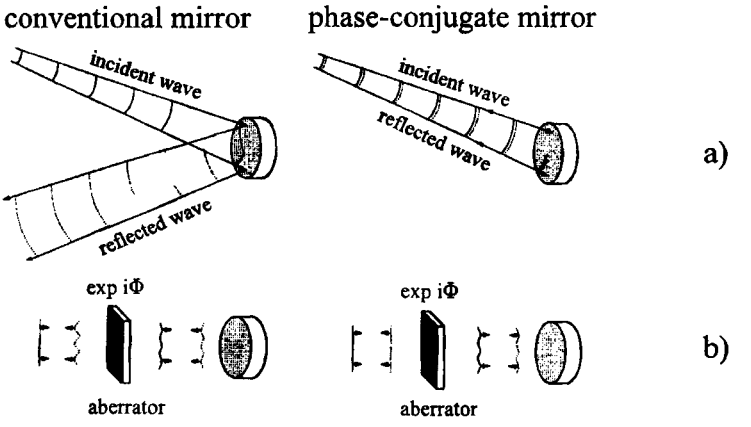

Fig. 16.22 Properties of a conventional mirror and a phase-conjugate mirror [S.19].

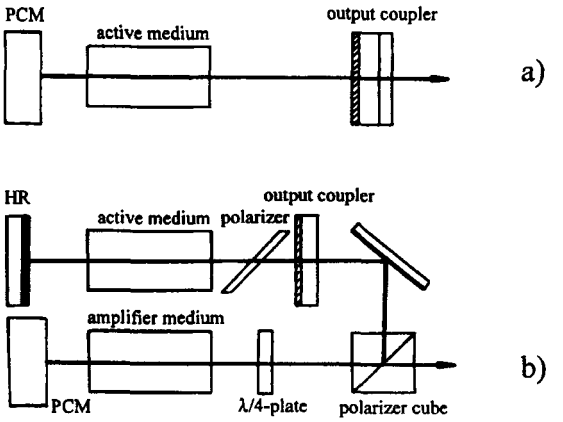

Fig. 16.23 Utilization of PCMs in laser systems. a) oscillator with phase-conjugate resonator mirror; b) PCM for compensating the phase distortions induced by the amplifiers.

Phase conjugation is present in all nonlinear optical processes since an intensity dependence of the index of refraction is sufficient to conjugate the phase. Phase conjugation has been extensively studied for three wave mixing, four wave mixing and stimulated scattering [4.232]. The most commonly used physical mechanism to realize PCMs is stimulated Brillouin scattering in gases and fluids. Before we discuss the physics of stimulated Brillouin scattering and the properties of PCMs based on this effect, let us first investigate how the characteristics of an optical resonator are affected by a phase-conjugate mirror.

16.4.2 Optical Resonators with a Phase-Conjugate Mirror

The basic properties of phase conjugate resonators can be evaluated by applying the ray transfer matrix formalism [4.213,4.216,4.222,4.223, 4.232]. If a Gaussian beam with a radius of curvature R and a beam radius w is incident on the PCM, its q-parameter q_1 reads:

$$\frac{1}{q_1} = \frac{1}{R} - i\frac{\lambda}{\pi w^2} \tag{16.52}$$

After reflection by the PCM the Gaussian beam must exhibit a conjugate phase, which means that the q-parameter q_2 of the reversed beam is given by:

$$\frac{1}{q_2} = -\frac{1}{R} - i\frac{\lambda}{\pi w^2} \tag{16.53}$$

Since the ABCD law $q_2=(Aq_1+B)/(Cq_1+D)$ must hold, the ray transfer matrix of the PCM is found to be:

$$M_{PCM} = \begin{pmatrix} A & B \\ C & D \end{pmatrix} = \begin{pmatrix} 1 & 0 \\ -2/R & 1 \end{pmatrix} \tag{16.54}$$

This is the well-known ray transfer matrix of a mirror with radius of curvature R. Therefore, a conventional mirror will act as a PCM, but only for incident fields whose phase curvatures match the curvature of the mirror. For a true PCM, phase conjugation takes place for arbitrary phase curvatures since the radius of curvature R of the PCM is induced by the field itself.

Using the Gaussian ABCD law for a resonator round trip, starting either on the PCM or the second, conventional mirror, one can derive the self-consistent Gaussian beams. For a resonator round trip, the Gaussian beams that are self-reproducing exhibit, like in conventional resonators, a wavefront that matches the radius of curvature ρ_1 of mirror 1. However, there is no constraint on the beam radius w_1 and an infinite number of Gaussian beams thus exist that represent eigensolutions of the phase-conjugate resonator (Fig. 16.24). For a Gaussian beam with radius w_1 on mirror 1, the following relations hold:

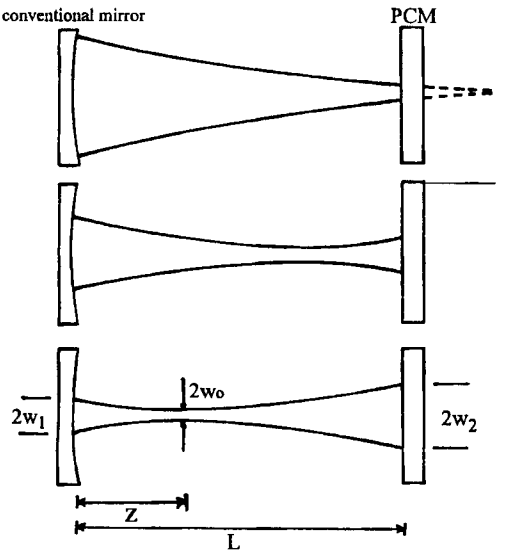

Fig. 16.24 Gaussian beams that exhibit a constant phase on mirror 1 are eigensolutions for the round trip in the resonator with an ideal phase-conjugate mirror 2.

Rayleigh range : $$z_0 = \frac{\pi w_1^2/\lambda}{1 + [\pi w_1^2/(\lambda \rho_1)]^2} \tag{16.55}$$

beam waist radius : $$w_0 = \sqrt{z_0 \lambda/\pi} \tag{16.56}$$

distance of waist from mirror 1 : $$z = z_0 \sqrt{\pi w_1^2/(\lambda z_0) - 1} \tag{16.57}$$

Using these relations, the radius of curvature R on the PCM and the beam radius w_2 can be easily obtained. The phase conjugation generates a freedom of stability constraints. Regardless of the mirror spacing and the curvature of mirror 1 we can always find self consistent Gaussian beams and the resonator will never become unstable. Another class of eigensolutions for the phase conjugate resonator can be found by applying the self-consistent field analysis to two round trips. It follows that electric fields exhibiting arbitrary amplitude and phase distributions on mirror 1 are exactly reproduced after two round trips, a result that can be easily verified by tracking a spherical wave through the resonator.

Which field distribution establishes itself in a real phase conjugate resonator depends on the physical process used for phase conjugation (e.g. the reflectance depends on the beam quality) and the size of apertures that are generally placed inside the PCR to control the transverse mode spectrum. It was shown both theoretically and experimentally that by using an apodized aperture with a Gaussian transmission (i.e. imposing a Gaussian reflectivity profile on the PCM, or generating a radial gain profile) only one self-consistent Gaussian beam is found [4.232]. Furthermore, the nonlinear nature of phase conjugation leads to transverse mode discrimination.

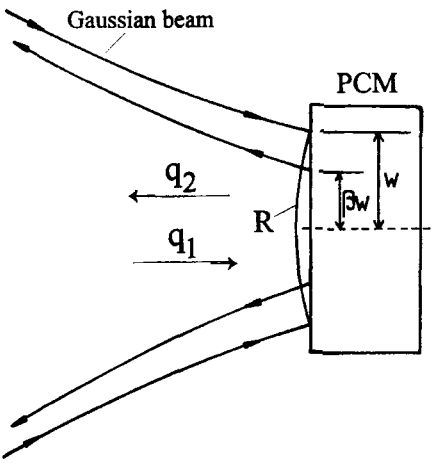

Fig. 16.25 A Gaussian beam is reflected by a real PCM. The beam radius w is reduced by a factor β.

Since the slopes of a beam incident on the PCM contain less power per unit area than its center, the reflectance of a PCM based on a nonlinear optical process is lower in the periphery of the beam. In addition to the reversal of the wavefront, a second characteristic of a real PCM, therefore, is the reduction of the beam diameter. For a Gaussian beam with beam radius w at the PCM (Fig. 16.25), it is reasonable to assume that the reflected beam is still Gaussian, with a beam radius that is reduced by a factor β (with $0<\beta<1$) [4.212,4.223]. The factor β is an empirical parameter that depends on the physical properties of the PCM and the intensity of the incident beam. The additional constraint on the beam size selects one well-defined Gaussian beam as the fundamental eigenmode of the phase conjugate resonator. Although the combination of wavefront reversal and beam size reduction is definitely a model too idealized to describe the properties of a real phase conjugate mirror, this description was found to be useful to theoretically predict the beam propagation inside phase-conjugate resonators (see Fig. 16.25).

In the following we will discuss this model in more detail [4.223]. According to Fig. 16.25, the q-parameters of the Gaussian beam with wavelength λ before and after reflection by the PCM are given by:

$$\frac{1}{q_1} = \frac{1}{R} - \frac{i\lambda}{\pi w^2} \tag{16.58}$$

$$\frac{1}{q_2} = -\frac{1}{R} - \frac{i\lambda}{\pi\beta^2 w^2} \tag{16.59}$$

If the PCM is used as a resonator mirror, the q-parameter q_2 must transfer into q_1 after one round trip. For a general resonator, the ray transfer matrix $\boldsymbol{M}$ for the round trip, starting at the PCM (but not incorporating it), is given by (Fig. 16.25):

$$\boldsymbol{M} = \begin{pmatrix} A & B \\ C & A \end{pmatrix} \tag{16.60}$$

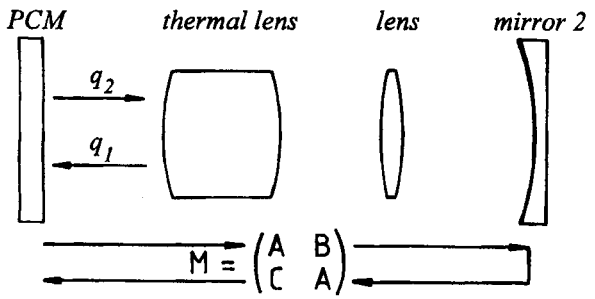

Fig. 16.26 Phase-conjugate resonator with round trip ray transfer matrix $\boldsymbol{M}$, starting at the PCM. Arbitrary ABCD-type optical elements can be placed inside the resonator.

Application of the ABCD-law:

$$q_1 = \frac{Aq_2 + B}{Cq_2 + A} \tag{16.61}$$

yields for the wavefront curvature R and the beam radius w of the self-consistent Gaussian beam at the PCM (going in):

$$R = \frac{B}{A} \tag{16.62}$$

$$w = \sqrt{\frac{\lambda B}{\pi \beta}} \tag{16.63}$$

With the knowledge of the Gaussian beam parameter at the PCM, the beam diameter at any plane inside the resonator can be calculated by using the well-known propagation law of Gaussian beams. Let us assume that the ray transfer matrix for the transit from the PCM to the considered plane is given by:

$$\boldsymbol{M}^* = \begin{pmatrix} A^* & B^* \\ C^* & D^* \end{pmatrix}$$

The beam radius w^* at this plane then reads:

$$w^{*2} = (A^* \beta w)^2 - 2A^* B^* \frac{\beta^2 w^2}{R} + \left(\frac{B^* \beta w}{R}\right)^2 + \left(\frac{B^* \lambda}{\pi \beta w}\right)^2 \tag{16.64}$$

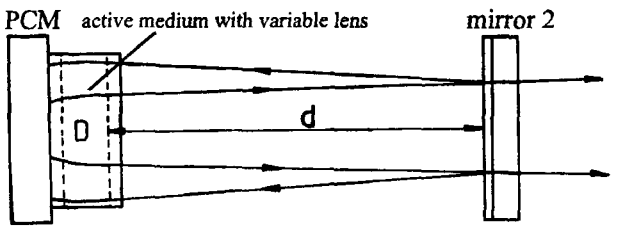

Fig. 16.27 Phase-conjugate resonator with an active medium exhibiting a variable refractive power D. The PCM is attached to the active medium. The broken, vertical lines indicate the principal planes of the lens. Mirror 2 is a flat output coupler.

In a preferred arrangement, the PCM is placed as close as possible to the lens medium as depicted in Fig. 16.27. For convenience we treat the active medium as a thin lens attached to the PCM. Starting at the PCM, the ray transfer matrix for the round trip reads:

$$M = \begin{pmatrix} 1-2dD & 2d \\ -2D(1-dD) & 1-2dD \end{pmatrix} \tag{16.65}$$

Equations (16.62) and (16.63) yield for the parameters of the Gaussian beam:

$$R = \frac{2d}{1-2dD} \quad , \quad w = \sqrt{\frac{2d\lambda}{\pi\beta}} \tag{16.66}$$
$$\tag{16.67}$$

Application of (16.64) with $A^*=1-dD$ and $B^*=d$, yields for the beam radius w^* at the output coupling mirror:

$$w^* = \sqrt{\frac{d\lambda}{2\pi}\,\frac{1+\beta^2}{\beta}} \tag{16.68}$$

The beam radii w and w^* at the mirrors remain constant as the refractive power D of the lens is varied. In the thin lens approximation used, this means that the mode volume of the Gaussian beam in the active medium is constant as well. Regardless of the refractive power, the PCR is always stable. This can also be demonstrated by calculating the g-parameters of the equivalent lens resonator. The combination of the PCM and the variable lens is equivalent to a conventional mirror with radius of curvature:

$$\rho = \left(\frac{1}{R} + D\right)^{-1} \tag{16.69}$$

Thus the equivalent g-parameters of the two mirrors (mirror 1 is the PCM-lens combination) are given by:

$$g_1^* = 1 - d(1/R + D) = \frac{1}{2} \tag{16.70}$$

$$g_2^* = 1 \tag{16.71}$$

The equivalent resonator is semi-confocal and remains at the same location in the stability

diagram. Unfortunately, this resonator scheme only provides a relatively small Gaussian beam radii in the active medium (for $d=1m$ and $\lambda=1\mu m$, the beam radii are on the order of 1mm). Larger Gaussian beam radii can be attained by separating the active medium from the PCM and incorporating a negative lens into the resonator (see Fig. 16.35). The separation may lead to a dependence of the Gaussian beam radii on the refractive power. However, the resonator always remains stable since the equivalent resonator remains in a stable zone. This can be shown for a general resonator set-up by using the ray transfer matrix (16.60) for a round trip. As was shown in Sec. 1.3, the ray transfer matrix for a resonator round trip starting at mirror 1 reads:

$$\boldsymbol{M}_{RT} = \begin{pmatrix} 2g_1^* g_2^* - 1 & 2L^* g_2^* \\ \dfrac{(2g_1^* g_2^* - 1)^2 - 1}{2L^* g_2^*} & 2g_1^* g_2^* - 1 \end{pmatrix} \tag{16.72}$$

where g_1^*, g_2^* are the equivalent g-parameters, and L^* is the equivalent length. The round trip matrix for the phase-conjugate resonator depicted in Fig. 16.26 is given by (using (16.54),(16.60), and (16.62):

$$\boldsymbol{M}_{RT} = \begin{pmatrix} 1 & 0 \\ -1/R & 1 \end{pmatrix} \begin{pmatrix} A & B \\ C & A \end{pmatrix} \begin{pmatrix} 1 & 0 \\ -1/R & 1 \end{pmatrix} = \begin{pmatrix} 0 & B \\ -1/B & 0 \end{pmatrix} \tag{16.73}$$

A comparison with (16.72) leads to the generalized stability condition for phase conjugate resonators:

$$g_1^* g_2^* = \frac{1}{2} \tag{16.74}$$

The first operation of a phase-conjugate resonator was reported in 1979 using a pulsed ruby laser and four-wave-mixing in a cell containing CS_2[4.213]. The CS_2 cell, which acts as the PCM, was pumped by two counterpropagating waves generated by a second ruby laser. Phase-conjugate resonators were also implemented in dye lasers and argon lasers using four wave-mixing or self-pumped photorefractive crystals [4.234]. In recent years, solid state lasers, excimer lasers, and dye lasers with intracavity stimulated Brillouin scattering (SBS) as the phase-conjugate process have been successfully operated [4.234-4.237,4.244-4.273] (Fig. 16.28).

Average output powers of tens of Watts have been demonstrated using Nd:YAG lasers utilizing SBS in liquids (CCl_4, Acetone, CS_2) and gases (CH_4, SF_6). An average output power of 27 W and 50W have been reported for Nd :YAG and Nd:YALO laser oscillators, respectively, both with a phase-conjugate mirror using SBS in SF_6 [4.262,5.268, 4.272].

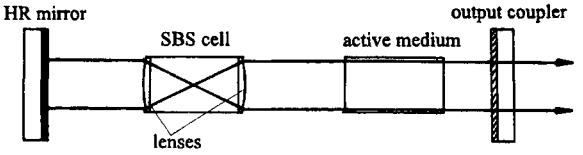

Fig. 16.28 A phase-conjugate resonator employing a SBS cell. Laser oscillation first occurs between the two conventional mirrors until the SBS threshold is exceeded.

The advantage of SBS is its self-pumping nature; no additional pump waves are required to initiate phase-conjugation. Unfortunately, the PCMs based on SBS exhibit a high threshold power on the order of 10 kW, which means that the phase-conjugate resonators can only be operated in a Q-switch mode with typical pulse lengths on the order of 10-100ns. Lower threshold powers are possible by using multiple SBS cells or tapered fibers [4.274].

16.4.3 Phase-Conjugate Resonators using SBS

Brillouin scattering is caused by the interaction of the incident field with the periodic density variations generated by a sound wave (Fig.16.29). For a monochromatic field with wavelength λ_0 incident at an angle θ with respect to the propagation direction of the sound wave, maximum scattering is observed if the fields scattered at the different density maxima interfere constructively (Bragg condition):

$$2\,\Lambda\,\sin\theta = \lambda_0 \tag{16.75}$$

where Λ is the wavelength of the sound wave.

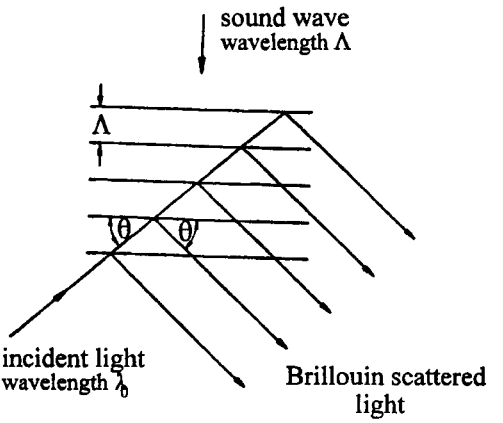

Fig. 16.29 Brillouin scattering of light by a sound wave.

Since the sound wave propagates with a speed V, the frequency of the scattered light is shifted by the Brillouin shift $\Delta\nu_B$ with respect to the incident frequency ν_0 due to the Doppler effect:

$$\Delta\nu_B = \pm\, \nu_0\, 2\, \frac{V}{c}\, \sin\theta \tag{16.76}$$

where c is the speed of light in the medium and the upper sign holds for sound waves propagating towards the incoming wave vector. Since the speed of sound V is on the order of 100 m/s in gases and 1,000 m/s in liquids, the relative frequency shift ν/ν_0 is very small (10^{-6}-10^{-5}). The sound waves are a manifestation of the thermal energy in the medium which means that all propagation directions and wavelengths down to a cut-off wavelength are present. Therefore, the incident electric field is scattered under all angles and the frequency is broadened and shifted according to (16.67). This scattering process is referred to as *spontaneous Brillouin scattering*.

If the intensity of the incident light is sufficiently high, the sound wave that scatters light is produced by the light itself (*stimulated Brillouin scattering (SBS)*). The physical process involved is electrostriction, the variation in volume due to an applied electric field. For SBS, the frequency of the scattered light is always reduced so that only the negative sign in (16.76) applies. If I_{in} denotes the intensity incident upon the SBS medium and I_{out} is the scattered intensity, the following coupled equations hold for the change of the intensities along the propagation distance z in the medium (assuming plane waves, a stationary sound wave, and pulse durations greater than the decay time of the sound wave):

$$\frac{dI_{in}}{dz} = -g_B\, I_{in}\, I_{out} - \alpha\, I_{in} \tag{16.77}$$

$$\frac{dI_{out}}{dz} = -g_B\, I_{in}\, I_{out} + \alpha\, I_{out} \tag{16.78}$$

with g_B : gain coefficient [cm/GW]
α : absorption loss coefficient [1/cm]

The gain coefficient, a characteristic of the medium (Table 16.6), is proportional to the frequency shift $\Delta\nu_B$ and thus maximum for backscattering ($\theta=\pi$). If we assume that the reflectivity generated by Brillouin scattering is low and the medium is loss-free, the incident intensity can be considered as being constant inside the medium. Equation (16.78) then yields for the reflected intensity:

$$I_{out} \sim \exp[g_B\, I_{in}\, s] \sim G \tag{16.79}$$

where s is the interaction length within which stimulated Brillouin scattering occurs.

Since the reflected wave is amplified with the gain factor G and the gain coefficient is maximum for backscattering, the incident wave with frequency ν_0 is reversed and exhibits the frequency:

$$\nu_B = \nu_0 \left(1 - 2\frac{v}{c}\right) \tag{16.80}$$

Although the gain factor, according to (16.79), seems to be a function of the incident intensity, the reflectance of a real SBS cell depends on the power P_{in} of the input beam since the beam is focused into the cell. This becomes understandable if we consider an incident beam with a radius w and a beam propagation factor M^2 focused into the SBS medium to a spot radius w_0 (Fig. 16.30). If the incident power is not too high, efficient scattering can only occur within an interaction length s that is x times larger than the Rayleigh range z_0 (Fig. 16.33) [4.255]:

$$s = x \frac{\pi w_0^2}{\lambda_0 M^2} \tag{16.81}$$

where the factor x depends slightly on the intensity. By using the relation $I_{in} = P_{in}/(\pi w_0^2)$ and inserting (16.81) into (16.79), the reflectance R of the SBS cell reads:

$$R = \frac{I_{out}}{I_{in}} \sim \exp\left|\frac{x\, g_B\, P_{in}}{\lambda_0 M^2}\right| \tag{16.82}$$

The pump power required to attain a reflectivity of the SBS cell in the percent range is defined as the threshold pump power, with:

$$P_{th} = \frac{C}{x} \frac{\lambda_0 M^2}{g_B} \tag{16.83}$$

where the ratio C/x was determined experimentally to be on the order of 10 [S.19].

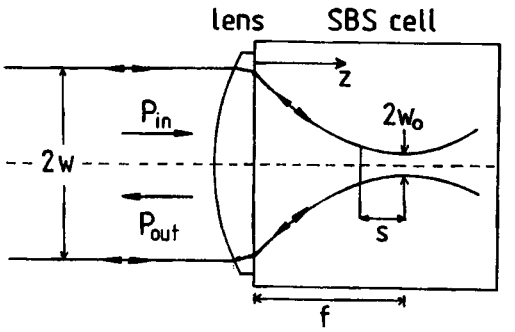

Fig. 16.30 Focusing of a laser beam into a SBS cell.

Keep in mind that the term "threshold" is physically not correct since SBS is also present at low pump powers, but with negligible efficiency. Typical threshold powers are in the range of 10-100kW which means that pulsed lasers are needed to reach noticeable reflectances. If a pulse duration of 30ns is used, the threshold pump power of 100kW corresponds to a beam energy of 3mJ. Note that the threshold becomes higher for higher order transverse modes. If the SBS cell is used as a resonator mirror, it can provide transverse mode discrimination such that the fundamental mode exhibits the lowest loss. The threshold defined by (16.83) holds only for cw-irradiation. If the pulse duration of the incident beam is on the same order of magnitude as the phonon lifetime τ_B, the threshold pump power can be several times higher. Table 16.6 lists gain coefficients, phonon lifetimes and threshold powers (16.83) for different SBS media. Measured reflectances for different SBS media are presented in Fig. 16.31.

Table 16.6 Gain coefficient g_B, phonon lifetime τ_B, and threshold power P_{th}, according to (16.83), of different SBS media ($\lambda_0=1\mu m$, $M^2=1$, $C/x=10$) [4.232,4.242,4.266,S.19,S.20].

Medium	g_B[cm/GW]	τ_B [ns]	P_{th} [kW]
H_20	5	---	200
CCl_4	6	0.6	167
$C_2Cl_3F_3$	6	0.84	167
Methanol	13	0.13	58
Benzene	13	---	58
SF_6	14	17.3	71
C_2F_6	18	6.6	55
Acetone	20	2.1	50
CO_2	20	10	50
CS_2	130	4.9	8

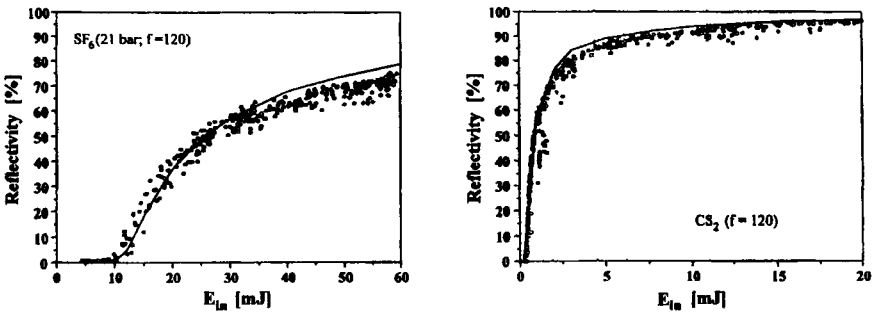

Fig. 16.31 Measured energy reflectance of two different SBS media [4.266]. The beam of a single longitudinal mode Q-switched Nd:YAG laser in fundamental mode operation was focused into the cells using a focal length of f=120mm. The minimum spot diameter in the cells was 100μm, the duration of the laser pulses was 25ns (FWHM), and the linewidth was 100MHz. The threshold input powers are: SF_6: 440kW; CS_2: 14kW. The solid lines are theoretical curves calculated with the model described in [4.255].

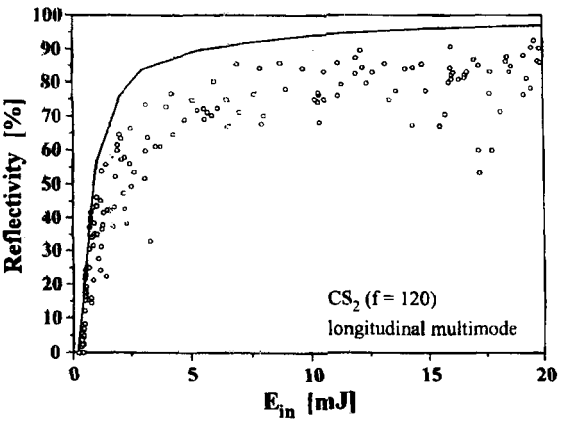

Fig. 16.32 Measured energy reflectance of CS_2 for a small coherence length of the incident Nd:YAG laser beam [4.266]. The same laser as in Fig. 16.31 was used, but with operation in longitudinal multimode. Compare this graph with the lower left graph of the previous picture to see the influence of the coherence length on the SBS reflectance. The solid line is the theoretical reflectance for single longitudinal mode operation, calculated with the model described in [4.255].

An important requirement for efficient SBS is a coherence length of the incident beam that is much greater than the interaction length s in the SBS cell (Fig. 16.32). This is necessary since the sound wave grating is generated by the interference of the incident and the reflected light wave. To accomplish this, the beam can either be focused tighter into the SBS cell or the coherence length can be increased with interference filters.

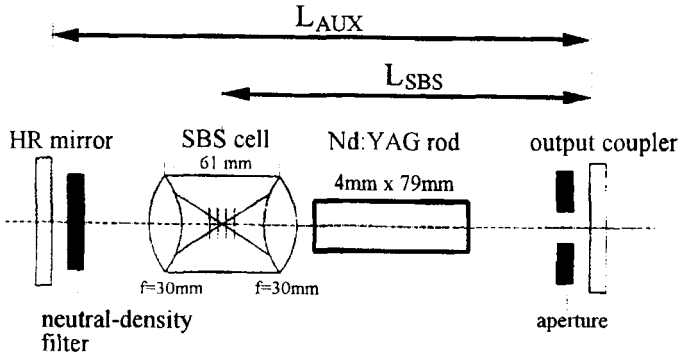

Fig. 16.33 A pulsed Nd:YAG laser with a SBS cell containing SF_6 at a pressure of 20 bar. The system uses an auxiliary resonator to reach the SBS threshold. An average output power of 10W in a near diffraction limited beam was obtained (pump pulse duration: 0.2ms, pump energy per pulse: 42J, L_{AUX}=1.8m, L_{SBS}=1.2m) [4.252] (© OSA 1992).

If the SBS cell is to replace a conventional mirror in a laser resonator it is necessary to use an auxiliary resonator to reach and exceed the threshold of the SBS cell. The necessary intracavity powers on the order of 10kW can be attained by either placing a Q-switch into the auxiliary resonator [4.211,4.218,4.244], or by using the Q-switching properties of the SBS cell itself [4.215,4.237,4.250,4.268,4.272]. An SBS Nd:YAG laser using the latter technique is depicted in Fig.16.33 [4.252]. The laser rod is pumped in a pulsed mode with a pump pulse duration of 0.2ms and a pump energy of 42J. At a repetition rate of 45Hz this phase-conjugate laser resonator provides a near diffraction limited output beam with an average output power of 10W. Between two and three pulses with a FWHM duration of 30ns were observed per pump pulse. Compared to a conventional resonator in multimode operation with the same pumping conditions, the efficiency was 65%. The neutral-density filter is needed to prevent stable laser oscillation in the auxiliary resonator (the filter can be removed if a partially reflecting rear mirror is used). By using a pump cavity that generated a peaked radial gain profile in the Nd:YAG rod, fundamental mode operation was also observed without the mode-control aperture.

In order to achieve efficient operation of a SBS laser resonator it is crucial to meet two design criteria. The optical length L_{SBS} of the SBS resonator and the optical length L_{AUX} of the auxiliary resonator have to be matched so that both resonators share axial mode frequencies. This ensures a smooth transition when the laser oscillation switches from the auxiliary resonator to the SBS resonator. Furthermore, the Brillouin shift should be multiples of the frequency spacing between the axial modes of the SBS resonator. This leads to the following two design equations:

$$\Delta\nu_B = n \frac{c_0}{2L_{SBS}} \quad , \quad n = 1,2,3,... \tag{16.84}$$

$$\Delta\nu_B = m \frac{c_0}{2L_{AUX}} \quad , \quad m = 2,3,4,... \tag{16.85}$$

where c_0 is the speed of light in vacuum. For SF_6 at 20 bar, the Brillouin shift is 250MHz. The shortest resonator (n=1,m=2) exhibits the effective lengths L_{AUX}=1.2m and L_{SBS}=0.6m. In addition, there is experimental evidence that the transverse mode structure of the two resonators should be matched too. This can be accomplished by an appropriate choice of the curvature of the high reflecting mirror. In addition, the auxiliary resonator must be stable over the whole refractive power range of the active medium, since the thermal lens is not compensated until the SBS cell becomes reflective.

At present, Nd:YAG lasers employing SBS resonator mirrors provide average output powers in excess of 50W in a near diffraction-limited output beam [4.272]. In order to achieve a high efficiency in fundamental mode operation it is necessary to adapt the Gaussian beam diameter to the diameter of the active medium. Although SBS oscillators have to be chosen long to meet the design criteria (16.84) and (16.85), the Gaussian beam fills only a fraction of the active volume. By inserting a negative lens into the resonator, Gaussian beam diameters in excess of 5mm can be realized in the active medium as the

measured and the calculated beam diameters in Fig. 16.34 illustrate [4.267]. The resonator set-up depicted meets (16.84) and (16.85) with n=2 and m=3 and a Brillouin shift of 250MHz (SF_6 at 20 bar). Note that the measured beam diameters in the medium are larger than predicted by the Gaussian beam propagation model described in (16.58)-(16.64), a discrepancy that cannot be explained satisfactorily by gain saturation.

Figure 16.35 presents results reported for a flashlamp-pumped phase-conjugate Nd:YAG laser oscillator using SF_6 at 20 bar as the SBS medium. This laser provides a maximum average output power of 27W in TEM_{00} mode operation [4.262,4.268]. Figure 16.35a shows one of the resonator designs used including the calculated fundamental mode beam diameter using the Gaussian beam propagation model (Eqs. (16.58)-(16.64)) in the limit β-->1. By using a slightly modified resonator scheme, a maximum output power of 27W was achieved at an electrical pump power of 3.9kW and a repetition rate of 50Hz, corresponding to a total efficiency of 0.7% (Fig. 16.35b).

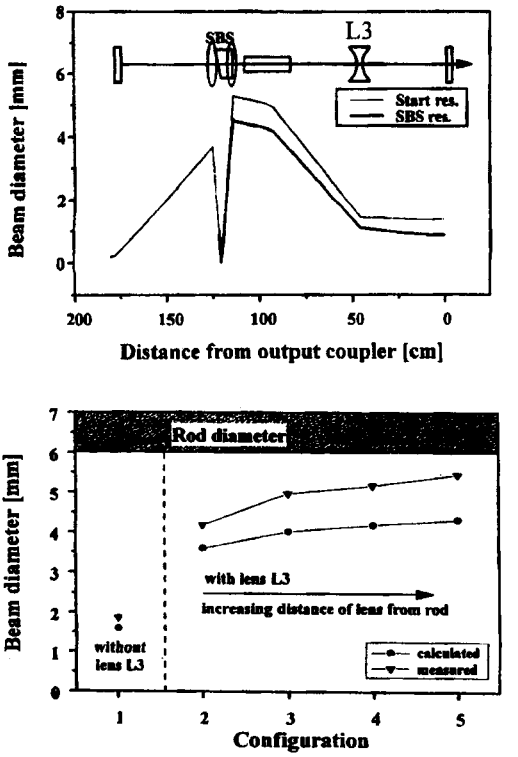

Fig. 16.34 Measured and calculated beam diameters for different phase-conjugate resonators using SF_6 at 20 bar as the SBS medium. The different configurations differ in the position of the -200mm lens L3. The upper graph depicts configuration 5. The beam diameters of the SBS resonator were calculated with (16.64) in the limit β-->1 (pump power: 390W, focal length of the rod: 84cm) [4.267].

The modulation of the temporal intensity profile of one laser pulse is due to the Brillouin shift of 250 MHz resulting in periodic spikes with a spacing of 4ns (Fig. 16.35c). A measurement of the beam quality using a moving knife edge (see Sec. 24.1) yielded a beam propagation factor of M^2=1.2 over the whole output power range.

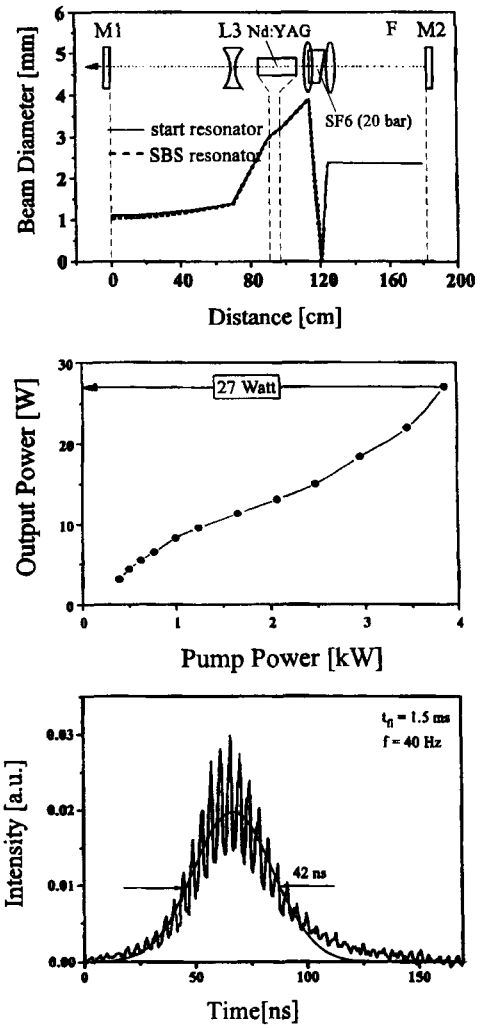

Fig. 16.35 A pulsed, phase-conjugate Nd:YAG rod laser using SBS in SF_6. (rod diameter: 4mm, rod length: 79mm, refractive power of rod: 1.1 diopter per kW of pump power, pump pulse duration: 1.5ms, pump energy: 77J, repetition rates: 10-50Hz). a) one of the resonator set-ups used showing calculated beam diameters, b) measured average output power as a function of the pump power, c) temporal emission profile of one laser pulse at a pump power of 2.8kW [4.262,4.268] (© IEEE 1998).

Higher output powers in the multi-100W range have already been realized by using the SBS cell in amplifier chains [4.259,4.263-4.265,4.273]. The Gaussian beam of a low power Q-switch oscillator with average output powers in the Watt range is used to generate high powers via amplification in one, two or more amplifier rods. In this arrangement the SBS cell is used to compensate for phase distortions induced by the amplifiers. The set-up depicted in Fig. 16.36 provides average output powers between 20 W and 215 W with beam propagation factors M^2 between 1.7 and 2.8 [4.264].

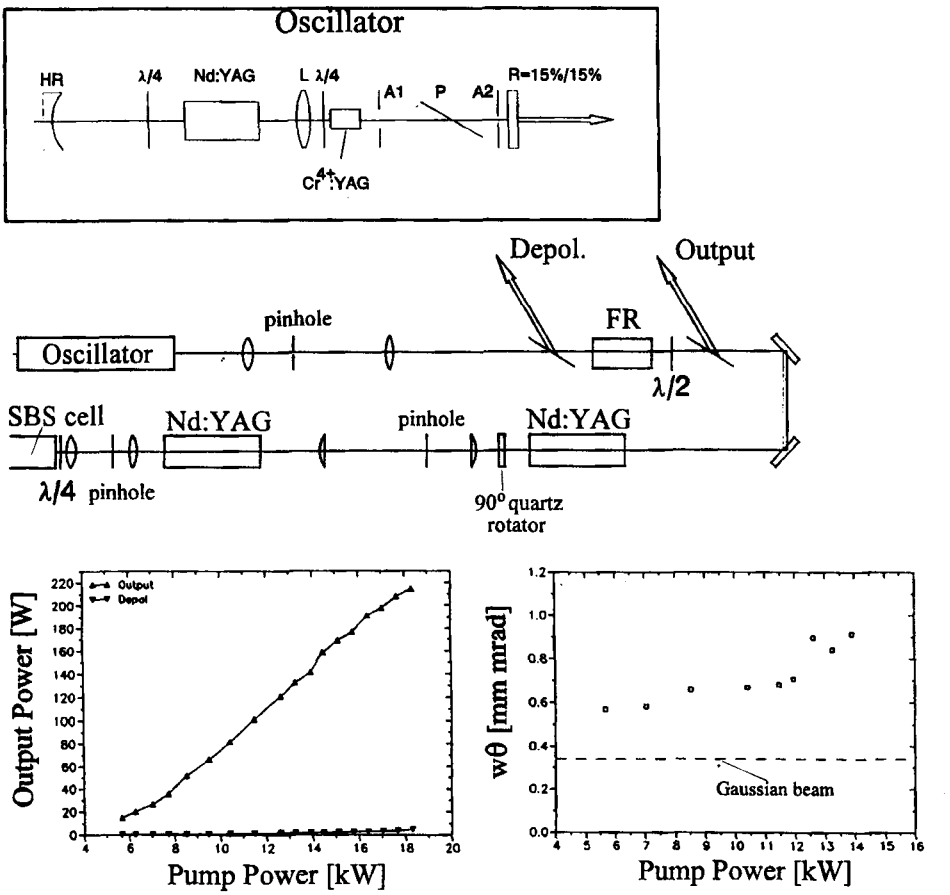

Fig. 16.36 Pulsed Nd:YAG laser with two amplifiers and an SBS cell containing CS_2. The upper graphs show the laser set-up including a schematic of the Q-switch oscillator (FR: Faraday rotator, P: polarizer, A: aperture, L: lens, λ/4: quarter wave plate, λ/2: half-wave plate, rod dimensions: 6"x3/8"). The oscillator, with Cr^{4+}:YAG as a passive Q-switch, provides 20 Q-switch pulses per pump pulse with an average output power of 3W (pump pulse duration: 0.5ms, pump pulse repetition rate: 100Hz, laser pulse duration: 200ns). The lower graphs present the average output power and the beam parameter product (waist radius w x half angle of divergence θ, 86.5% power content) as a function of the total electrical pump power [4.264] (© SPIE 1996).

Part V

Special Resonator Concepts